

Modeling the emission spectra of polycyclic aromatic hydrocarbons by recurrent fluorescence

Damien Borja,^{1,2} Florent Calvo,² Pascal Parneix,¹ and Cyril Falvo^{1,2}

¹⁾*Université Paris-Saclay, CNRS, Institut des Sciences Moléculaires d'Orsay, 91405, Orsay, France*

²⁾*Université Grenoble-Alpes, CNRS, LIPhy, 38000 Grenoble, France*

(*Electronic mail: cyril.falvo@universite-paris-saclay.fr)

(Dated: 6 January 2026)

Recurrent fluorescence (RF) is an important relaxation mechanism in polycyclic aromatic hydrocarbons (PAHs), which could stabilize them and contribute to the production of aromatic infrared bands that are observed in the infrared spectra of the interstellar medium (ISM). In this theoretical work, a statistical model of relaxation by recurrent fluorescence is formally developed, including Herzberg-Teller and Duschinsky rotation effects as well as a full account of vibrational progressions. Using canonical and harmonic approximations, the RF rate constants can be determined from the transition dipole moment time autocorrelation functions. Application to the naphthalene, anthracene, and pyrene cations is presented based on quantum chemical inputs obtained from time-dependent density-functional theory. For these highly symmetric molecules, the low-lying, symmetry-forbidden electronic excited states are predicted to contribute possibly even more than higher energy, non-forbidden states. Such an unexpected contribution could increase the cooling efficiency of PAHs and, in turn, stabilize them further under the highly ionized environments of the ISM.

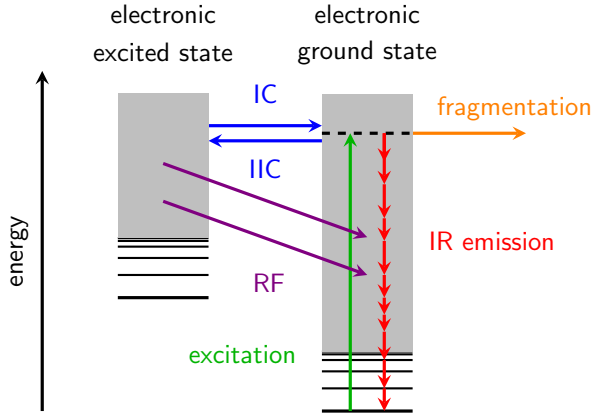


FIG. 1. Jablonski diagram showcasing some of the most important processes involved in the stochastic heating mechanism: initial excitation, IR photon emission, fragmentation, internal conversion (IC), inverse internal conversion (IIC) and recurrent fluorescence (RF).

I. INTRODUCTION

The presence of polycyclic aromatic hydrocarbons (PAHs) in the interstellar medium (ISM) was hypothesized over 40 years ago to explain the observation of the so-called aromatic infrared bands (AIBs).^{1,2} This hypothesis was recently supported by the detection of large quantities of cyanonaphthalene compounds in the Taurus Molecular Cloud 1 region.³

Such a detection raises questions about the stability of small PAHs in the interstellar medium, due to their likely vulnerability to highly energetic radiation.⁴ Shortly after their existence was theoretically postulated, it was suggested that small PAHs might undergo a specific radiative relaxation process called recurrent fluorescence (RF), also known as Poincaré fluorescence,⁵ which would enhance their stability. Following the transient heating mechanism,⁶ in which PAH molecules absorb UV or visible radiation, they can be excited to high-energy electronic states. Individual molecules can then rapidly undergo internal conversion (IC), transferring electronic excitation into vibrational energy in the electronic ground state. Subsequently, relaxation can proceed further through the emission of IR photons, thereby causing the AIBs.

Among the various possible relaxation mechanisms taking place upon transient heating, which notably include fragmentation, RF can occur when sufficient energy remains in the vibrational modes of the molecule to excite a low-lying electronic excited state through inverse internal conversion (IIC).⁷ Subsequent relaxation to the electronic ground state proceeds via electronic flu-

rescence in the near-IR or visible regions (see Fig. 1). This alternative mechanism is not observed in dense media, as collisions with the surrounding environment dissipate energy faster than the characteristic IIC timescale, yet it is relevant under low densities. RF was directly observed in the Zare group⁷ as delayed electronic luminescence following multi-photon IR photon absorption in collision-free conditions and taking place over time scales of a few μ s. It was also proposed later by Léger and co-workers⁵ as a possibly important mechanism occurring in PAH molecules in the ISM, providing an additional radiative relaxation pathway enhancing their stability. More recently, it has also been suggested that RF could contribute to the near-IR emission continuum observed in the ISM.⁸

A large number of dedicated experiments on the relaxation kinetics of PAHs have relied on ion traps^{9–11} and storage rings.^{12–19} These setups replicate ISM-like conditions by providing a low-density environment, enabling the study of collisional-free relaxation of hot PAH cations over long timescales reaching tens of milliseconds. The internal energy remaining in the molecular ions is typically monitored by measuring the occurrence of dissociation byproducts during the relaxation. In particular for PAHs, in the excitation energy range relevant for astrochemistry (< 13.6 eV), such byproducts usually consist of atomic hydrogen and acetylene.^{20–22} These experiments have revealed that multiple relaxation mechanisms, including RF, compete to dissipate energy, thereby providing an indirect access to the RF process.

The RF-delayed emission mechanism was also directly observed by Saito and coworkers for naphthalene and antracene^{10,11} in the wavelength region between 500 and 850 nm, using various bandpass filters. These authors observed an emission profile comparable to the absorption spectrum in the short-wavelength side but with a stronger component in the long-wavelength side, whose origin remains unclear.

Already from its original conceptualization, RF has been identified as a statistical process and its theoretical framework has seen little advancement since the pioneering work of Nitzan and Jortner.^{23,24} These authors described RF as a vertical transition, using the Condon approximation applied to a microcanonical statistical population in the electronic excited state. This model has been applied to individual molecules^{25–27} and was shown to lead to blackbody-like emission spectra when applied to a broad molecular sample.²⁸ It was also recently improved to include the Herzberg-Teller (HT) contribution²⁹ in the transition dipole moment between the electronic ground and excited states.¹⁸ The HT coupling is known for strongly modifying the molecular absorption and emission profiles,³⁰ and in the context of RF, it was notably shown that the HT coupling can

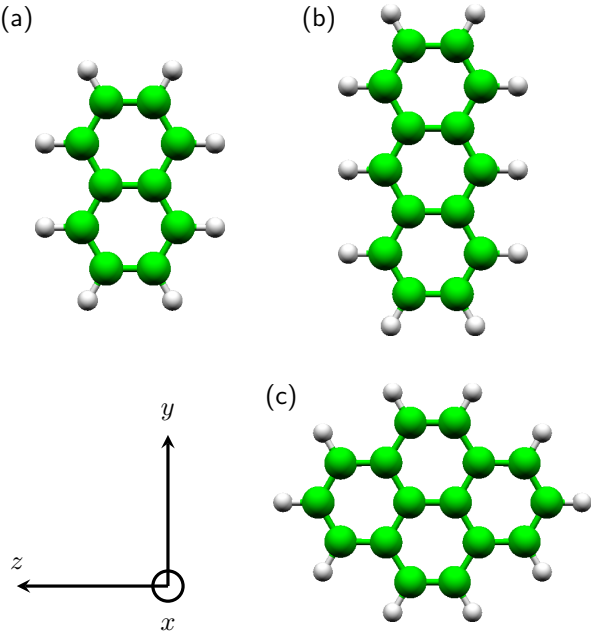


FIG. 2. PAH cations studied in this work. (a) Naphthalene; (b) anthracene; (c) pyrene, together with the reference frame used to identify appropriate symmetries.

increase the stability of cyanonaphthalene by strongly increasing the oscillator strength of the lowest electronic excited state. However, in the approach by Stockett and coworkers,¹⁸ the remaining vibrational energy in the electronic excited state is not considered and the effects of the vibrational structure of both electronic states are still ignored, hindering a more complete interpretation of the spectra measured by Saito *et al.*^{10,11}

The inclusion of the molecular vibrational structure in the modeling of absorption and emission spectroscopy experiments can be achieved by explicitly computing the Franck-Condon (FC) factors between the various vibronic states.^{31,32} This method is applicable for harmonic potential energy surfaces, with or without the Duschinsky rotation effects, as well as for anharmonic potential energy surfaces. Unfortunately, it is computationally tractable only for moderately large systems and for limited numbers of initial states. Alternatively, a more global method for determining the spectroscopic signature, based on the transition dipole moment time correlation function, is particularly efficient for harmonic systems at thermal equilibrium and can readily account for the Duschinsky rotation.^{33–35} To date, neither approach has been applied to the study of RF processes.

Many archetypal PAHs used to model the AIBs exhibit a high symmetry, and such is the case for the naphthalene (Np), anthracene (An), and pyrene (Py) cations depicted in Fig. 2, which all

fall into the D_{2h} point group. Symmetry plays a crucial role in the optical response of molecular systems, and can alone forbid excitations to specific electronic states.³⁶ In the (fairly large) Np^+ , An^+ , and Py^+ cations, the lowest-lying electronic excited state, commonly noted as D_1 , is most likely to be populated through the IIC mechanism in the statistical limit. However, D_1 is also a dark state and thus does not contribute to the emission spectrum, which explains why the current modeling of RF emission and its associated rate constants in such molecules have usually ignored this state, focusing exclusively on the second (bright) electronic excited state, D_2 .^{9,10,17} However, at finite internal energy, the excitation of vibrational modes with ungerade symmetry breaks the inversion symmetry of the molecules, possibly leading to a finite transition dipole moment, which could in turn enable the HT effect, confirming the importance of such processes to explain the stability of non inversion-symmetric molecules such as cyanonaphthalene.¹⁸ To the best of our knowledge, in the case of inversion-symmetric molecules like those depicted in Fig. 2, these effects have only been considered in a very recent study,³⁷ where RF is modeled as an average of vertical transitions from individual geometries extracted from *ab initio* molecular dynamics simulations. This approach naturally includes the symmetry breaking due to presence of internal energy but does not include all the HT effects, which manifest even in the absence of internal energy.

The present work pursues two main objectives. First, a new theoretical framework for relaxation by recurrent fluorescence emission in high-dimensional molecular systems is introduced, based on the harmonic approximation and explicitly accounting for both HT couplings and vibrational progressions. The approach relies on the calculation of the transition dipole moment time autocorrelation function, and a practical but accurate solution involving a canonical representation of the true microcanonical energy distribution. Second, the model is applied to quantify the contribution of symmetry-forbidden states in the inversion-symmetric Np^+ , An^+ and Py^+ cationic PAHs to their RF emission spectrum and the associated rate constants.

The article is organized as follows. In Sec. II, we present the theoretical model, from a general perspective first, before proceeding to a practical solution based on harmonic models. The results are introduced in Sec. III, discussed in the light of the importance of the D_1 states and their dependence on the PAH itself, and compared with existing experiments. Finally, conclusions are drawn in Sec. IV, together with some possible future extensions.

II. THEORETICAL MODEL FOR RF RELAXATION

A. Recurrent fluorescence differential rate constant

A nonrotating molecule is described by its electronic ground state $|g\rangle$ and one electronic excited state denoted by $|e\rangle$. Generalization to an arbitrary number of electronic states is straightforward and described in Appendix A. For both states $|g\rangle$ and $|e\rangle$, the vibrational dynamics is described by appropriate Hamiltonians H_g and H_e , respectively. Within the Born-Oppenheimer approximation, the total Hamiltonian H of the system is expressed as

$$H = H_g|g\rangle\langle g| + H_e|e\rangle\langle e|. \quad (1)$$

For a molecule with internal energy E relative to the fundamental vibronic state, the dimensionless differential RF rate constant is given by

$$k^{\text{RF}}(\omega; E) = \sum_{i,f} P_i(E) A_{if} \delta(\omega - \omega_{if}), \quad (2)$$

where i and f are the initial and final vibronic states, respectively, $P_i(E)$ the occupation probability of state i and $\omega_{if} = \omega_i - \omega_f$ is the transition frequency. In Eq. (2), the Einstein coefficient A_{if} for spontaneous emission is expressed as

$$A_{if} = \frac{\omega_{if}^3}{3\pi\epsilon_0\hbar c^3} |\mathbf{d}_{if}|^2, \quad (3)$$

where $\mathbf{d}_{if} = \langle i|\mathbf{d}|f\rangle$ is the transition dipole moment between the initial and final states. Using the expression of the Fourier transform of the delta function, the RF differential rate constant can be rewritten as

$$k^{\text{RF}}(\omega; E) = \frac{\omega^3}{3\pi\epsilon_0\hbar c^3} \int_{-\infty}^{+\infty} \frac{dt}{2\pi} \text{Tr}[\rho(E)\mathbf{d}(0) \cdot \mathbf{d}(t)] e^{i\omega t}, \quad (4)$$

where the trace acts over all vibronic states. In Eq. (4), the transition dipole moment is given by

$$\mathbf{d} = \mathbf{d}_{eg}|e\rangle\langle g| + \mathbf{d}_{ge}|g\rangle\langle e|, \quad (5)$$

where \mathbf{d}_{eg} and \mathbf{d}_{ge} are operators acting in the vibrational coordinates space. Within a microcanonical statistical model, the density matrix $\rho(E)$ is given by

$$\rho(E) = \frac{\delta(H - E)}{\Omega(E)}, \quad (6)$$

with $\Omega(E) = \text{Tr}[\delta(H - E)]$ is the density of vibronic states. The density matrix can be expanded over the two electronic states as

$$\rho(E) = \rho_g(E)|g\rangle\langle g| + \rho_e(E)|e\rangle\langle e|, \quad (7)$$

where the vibrational density matrices $\rho_g(E)$ and $\rho_e(E)$ are given by

$$\rho_i(E) = \frac{\delta(H_i - E)}{\Omega_g(E) + \Omega_e(E)}, \quad i = g, e. \quad (8)$$

The densities of vibrational states $\Omega_g(E)$ and $\Omega_e(E)$ in each electronic state are formally expressed using the trace over vibrational states Tr_v ,

$$\Omega_i(E) = \text{Tr}_v[\delta(H_i - E)] \quad i = g, e. \quad (9)$$

Therefore the total probability to be in the electronic excited state is given by

$$P_e(E) = \text{Tr}_v[\rho_e(E)] = \frac{\Omega_e(E)}{\Omega_g(E) + \Omega_e(E)}. \quad (10)$$

We next assume that fluorescence can only occur from the excited electronic state to the electronic ground state. The RF differential rate constant is thus written as

$$k^{\text{RF}}(\omega; E) = \frac{\omega^3}{3\pi\epsilon_0\hbar c^3} \int_{-\infty}^{+\infty} \frac{dt}{2\pi} \text{Tr}_v[\rho_e(E) e^{-iH_e t/\hbar} \mathbf{d}_{eg} e^{iH_g t/\hbar} \mathbf{d}_{ge}] e^{i\omega t}. \quad (11)$$

Solving the correlation function inside the integral of Eq. (11) directly in the microcanonical ensemble requires to compute explicitly the trace over vibrational states. This operation is computationally extensive, even under the harmonic approximation, and only feasible for systems with a very small number of degrees of freedom, especially when accounting for the Duschinsky effect that couples the various normal modes together. However, and following earlier suggestions,^{34,35} the calculation becomes significantly more tractable for harmonic systems governed by the *canonical* ensemble.

To proceed, the energy within each state is then assumed to follow a Boltzmann distribution at an effective canonical temperature $T_{\text{eff}}(E)$, rather than a delta-peaked distribution that is characteristic of the true microcanonical distribution, and while keeping this microcanonical distribution for determining the occupancy probability of the electronic ground and excited states. At any arbitrary energy E_0 , and for any electronic state i , the microcanonical temperature T_μ at thermal equilibrium is defined from the density of vibrational states as

$$\beta_\mu(E_0) = \frac{1}{k_B T_\mu} = \frac{\partial \ln \Omega_i}{\partial E} \bigg|_{E=E_0}. \quad (12)$$

The probability distribution $p_i(E)$ of energies in the microcanonical ensemble is a delta peak at energy E_0 , but becomes broad once in the presence of a thermostat. In the canonical ensemble at inverse temperature $\beta = 1/k_B T$, and for the very same electronic state, the corresponding probability distribution reads

$$p_i^{(T)}(E) \propto \Omega_i(E) e^{-\beta E}, \quad (13)$$

where the normalizing prefactor is the inverse of the canonical partition function.

For any given microcanonical energy E_0 , several choices are available for the effective canonical temperature $T_{\text{eff}}(E_0)$ based on the above probability distributions. One possibility consists in adjusting the maximum of the canonical distribution, $\max_E \{p_i^{(T)}(E)\}$, to the microcanonical energy value, thereby providing a first value for T_{eff} denoted as T_{max} . By differentiation of Eq. (13) it can be straightforwardly shown that the maximum of the distribution occurs when $T_{\text{max}} = T_\mu$.

Alternatively, instead of the maximum, the average $\langle E \rangle$ of the distribution can be adjusted to match the microcanonical energy, the corresponding equation $\langle E \rangle(T) = E_0$ being always well defined owing to the monotonic character of $\langle E \rangle(T)$. Unlike T_{max} , which is rooted in microcanonical statistics, the effective temperature T_{av} resulting from matching $\langle E \rangle$ to the required E_0 has a canonical perspective.

Except for classical harmonic systems in the large size limit, T_{max} and T_{av} generally differ from one another. However, and as will be shown below, this difference is rather small already for the present systems, and the choice of T_{av} as the effective canonical temperature turns out to be slightly more accurate than T_{max} .

Denoting simply $\beta_{\text{eff}} = 1/k_B T_{\text{eff}}$ the inverse effective canonical temperature, the differential RF rate constant is next rewritten as

$$k^{\text{RF}}(\omega; E) = \frac{\omega^3}{3\pi\epsilon_0\hbar c^3} P_e(E) \int_{-\infty}^{+\infty} \frac{dt}{2\pi} \frac{1}{Z_e(T_{\text{eff}})} C_{ge}(-t, t - i\beta_{\text{eff}}\hbar) e^{i\omega t}, \quad (14)$$

where the correlation function $C_{ge}(\tau_g, \tau_e)$ reads

$$C_{ge}(\tau_g, \tau_e) = \text{Tr}_v \left[e^{-iH_g \tau_g / \hbar} \mathbf{d}_{ge} e^{-iH_e \tau_e / \hbar} \mathbf{d}_{eg} \right]. \quad (15)$$

From this expression, the total RF rate constant is derived as

$$k_{\text{tot}}^{\text{RF}}(E) = \int_0^{\infty} d\omega k^{\text{RF}}(\omega; E). \quad (16)$$

At any physical temperature $T = 1/k_B \beta$, the equilibrium absorption cross-section can be obtained using a similar correlation function

$$\sigma^{\text{abs}}(\omega; T) = \frac{\pi\omega}{3\hbar\epsilon_0 c} \left(1 - e^{-\beta\hbar\omega}\right) \int_{-\infty}^{+\infty} \frac{dt}{2\pi} \frac{1}{Z_g(T)} C_{ge}(-t - i\beta\hbar, t) e^{i\omega t}, \quad (17)$$

where $Z_g(T) = \text{Tr}[e^{-\beta H_g}]$ is the equilibrium partition function in the electronic ground state. The same formalism provides the photoelectron spectra between the electronic ground state g of the neutral molecule and the electronic state e (which can also be an electronic ground state) of the corresponding cation by assuming a vertical transition. The spectral intensity is then proportional to

$$\mathcal{I}^{\text{PE}}(\omega; T) = \int_{-\infty}^{+\infty} \frac{dt}{2\pi} \frac{1}{Z_g(T)} C_{ge}^{\text{PE}}(-t - i\beta\hbar, t) e^{i\omega t}, \quad (18)$$

where $C_{ge}^{\text{PE}}(\tau_g, \tau_e)$ is given by

$$C_{ge}^{\text{PE}}(\tau_g, \tau_e) = \text{Tr}_v \left[e^{-iH_g\tau_g/\hbar} e^{-iH_e\tau_e/\hbar} \right]. \quad (19)$$

The calculation of the correlation function from Eqs. (15) and (19) requires the knowledge of the eigenvalues and eigenstates of the vibrational Hamiltonians H_g and H_e . In the general anharmonic case, this can only be achieved numerically and for small systems. However, the problem can be largely simplified under the harmonic approximation.

B. Harmonic model

Following Refs. 34 and 35, the harmonic approximation is used to obtain the differential RF rate constants. Within this approximation, the potential energy surface is expanded up to the second order around the electronic ground state equilibrium position and H_g is expressed as a function of the $n = 3N - 6$ normal mode coordinates $q_{g,i}$ and the conjugated momenta $p_{g,i}$, the total number of atoms being denoted as N . The Hamiltonian is then written as

$$H_g = \sum_i^n \frac{1}{2} (p_{g,i}^2 + \omega_{g,i}^2 q_{g,i}^2), \quad (20)$$

where $\omega_{g,i}$ denotes the set of ground state vibrational frequencies. In the electronic excited state, a similar expansion can be performed around the corresponding equilibrium position and the Hamiltonian is expressed as a function of the normal mode coordinates $q_{e,i}$ and the conjugated momenta $p_{e,i}$ as

$$H_e = \sum_i^n \frac{1}{2} (p_{e,i}^2 + \omega_{e,i}^2 q_{e,i}^2) + \hbar\omega_{eg}, \quad (21)$$

where $\omega_{e,i}$ now denotes the set of electronic excited state vibrational frequencies, with ω_{eg} being the adiabatic transition frequency connecting the two electronic states. Both sets of normal modes coordinates are linearly connected to each other,

$$\mathbf{q}_e = \mathbf{S}\mathbf{q}_g + \mathbf{K}, \quad (22)$$

where $\mathbf{q}_g = (q_{g,1}, q_{g,2}, \dots, q_{g,n})$ and $\mathbf{q}_e = (q_{e,1}, q_{e,2}, \dots, q_{e,n})$ are two n -tuples containing the electronic ground and excited states normal mode coordinates. In Eq. (22), \mathbf{S} is the Duschinsky rotation matrix defined as the projection of the electronic ground state normal mode coordinates on the electronic excited state normal mode coordinates and \mathbf{K} is the displacement vector corresponding to the difference in equilibrium positions in the electronic ground and excited states, expressed in the basis set of the electronic excited state normal mode coordinates. The detailed expressions of the matrix \mathbf{S} and the vector \mathbf{K} as a function of the electronic states potential energy surface parameters are given in Appendix B.

Within the harmonic approximation, the canonical partition function is readily obtained for any electronic excited state, e.g. as

$$Z_e(T_{\text{eff}}) = \prod_{i=1}^n \frac{1}{2 \sinh \beta_{\text{eff}} \hbar \omega_{e,i} / 2} \quad (23)$$

for the electronic excited state, and a similar expression for the electronic ground state. The transition dipole moment between the electronic ground and excited states can also be expanded linearly around the electronic ground state geometry as

$$\mathbf{d}_{eg} = \mathbf{d}_{ge} = \mathbf{d}_g^0 + \sum_i \mathbf{d}_{g,i}^1 q_{g,i} = \mathbf{d}_g^0 + \mathbf{d}_g^1 \mathbf{q}_g, \quad (24)$$

where the three-dimensional vector \mathbf{d}_g^0 and the $3 \times n$ matrix \mathbf{d}_g^1 give the Franck-Condon and Herzberg-Teller contributions to the vibronic spectra, respectively. Alternatively, the transition dipole moment can be expanded linearly around the electronic excited state equilibrium geometry as

$$\mathbf{d}_{eg} = \mathbf{d}_{ge} = \mathbf{d}_e^0 + \mathbf{d}_e^1 \mathbf{q}_e. \quad (25)$$

Under this linear approximation, Eqs. (24) and (25) are thus connected to one another through

$$\mathbf{d}_g^0 = \mathbf{d}_e^0 + \mathbf{d}_e^1 \mathbf{K}, \quad (26)$$

$$\mathbf{d}_g^1 = \mathbf{d}_e^1 \mathbf{S}. \quad (27)$$

Following Ianconescu and Pollak,³⁴ the trace in Eq. (15) can be solved using the ket vectors in coordinate representation $|\mathbf{q}_g\rangle$ and $|\mathbf{q}_e\rangle$. Both sets of vectors are orthonormal and related to each other through

$$\langle \mathbf{q}_e | \mathbf{q}_g \rangle = \delta(\mathbf{q}_e - \mathbf{S}\mathbf{q}_g - \mathbf{K}). \quad (28)$$

The correlation function $C_{ge}(\tau_g, \tau_e)$ is formally given by

$$C_{ge}(\tau_g, \tau_e) = \int d^n \mathbf{q}_g d^n \mathbf{q}'_g \mathbf{d}(\mathbf{q}_g) \cdot \mathbf{d}(\mathbf{q}'_g) \langle \mathbf{q}_g | e^{-\frac{i}{\hbar} H_g \tau_g} | \mathbf{q}'_g \rangle \langle \mathbf{S} \mathbf{q}'_g + \mathbf{K} | e^{-\frac{i}{\hbar} H_e \tau_e} | \mathbf{S} \mathbf{q}_g + \mathbf{K} \rangle, \quad (29)$$

and in the harmonic approximation the matrix elements of the propagators can be computed using path integrals,³⁸ yielding

$$\langle \mathbf{q} | e^{-\frac{i}{\hbar} H \tau} | \mathbf{q}' \rangle = \sqrt{\frac{\det \mathbf{a}}{(2i\pi\hbar)^n}} \exp\left(\frac{i}{2\hbar} [\mathbf{q}^T \mathbf{b} \mathbf{q} + \mathbf{q}'^T \mathbf{b} \mathbf{q}' - 2\mathbf{q}^T \mathbf{a} \mathbf{q}']\right), \quad (30)$$

where the diagonal matrices \mathbf{a} and \mathbf{b} are given from their elements a_{ij} and b_{ij} as

$$a_{ij} = \delta_{ij} \frac{\omega_i}{\sin(\omega_i \tau)}, \quad (31)$$

$$b_{ij} = \delta_{ij} \frac{\omega_i}{\tan(\omega_i \tau)}. \quad (32)$$

Both \mathbf{a} and \mathbf{b} are defined for each electronic state g and e and depend on the parameters τ_g and τ_e . As in Ref. 34 the following $n \times n$ matrices are next introduced

$$\mathbf{A} = \mathbf{a}_g + \mathbf{S}^T \mathbf{a}_e \mathbf{S}, \quad (33)$$

$$\mathbf{B} = \mathbf{b}_g + \mathbf{S}^T \mathbf{b}_e \mathbf{S}, \quad (34)$$

$$\mathbf{E} = \mathbf{b}_e - \mathbf{a}_e, \quad (35)$$

providing a simplified expression for the correlation function as

$$C_{ge}(\tau_g, \tau_e) = \sqrt{\frac{\det \mathbf{a}_g \det \mathbf{a}_e}{(2i\pi\hbar)^{2n}}} e^{-i\omega_{eg} \tau_e} \int d^n \mathbf{q}_g d^n \mathbf{q}'_g \mathbf{d}(\mathbf{q}_g) \cdot \mathbf{d}(\mathbf{q}'_g) \times \exp\left(\frac{i}{2\hbar} [\mathbf{q}_g^T \mathbf{B} \mathbf{q}_g + \mathbf{q}'_g^T \mathbf{B} \mathbf{q}'_g - 2\mathbf{q}_g^T \mathbf{A} \mathbf{q}'_g + 2\mathbf{K}^T \mathbf{E} \mathbf{S}(\mathbf{q}_g + \mathbf{q}'_g) + 2\mathbf{K}^T \mathbf{E} \mathbf{K}]\right). \quad (36)$$

Following Ref. 35, we next introduce the unitary transformation

$$\mathbf{u} = \frac{1}{\sqrt{2}} (\mathbf{q}_g + \mathbf{q}'_g), \quad (37)$$

$$\mathbf{v} = \frac{1}{\sqrt{2}} (\mathbf{q}_g - \mathbf{q}'_g). \quad (38)$$

Using these variables, the scalar product of dipole moments vectors can be written as

$$\mathbf{d}(\mathbf{q}_g) \cdot \mathbf{d}(\mathbf{q}'_g) = \left(\mathbf{d}_g^0 + \frac{1}{\sqrt{2}} \mathbf{d}_g^1 \mathbf{u} \right)^2 - \frac{1}{2} (\mathbf{d}_g^1 \mathbf{v})^2. \quad (39)$$

Finally, solving the remaining Gaussian integrals provides an explicit form for the time correlation function C_{ge} as

$$C_{ge}(\tau_g, \tau_e) = \left[\left(\mathbf{d}_g^0 - \sum_{kp} \mathbf{d}_{g,k}^1 C_{kp}^{-1} \Gamma_p \right)^2 + \frac{i\hbar}{2} \sum_{kp} \mathbf{d}_{g,k}^1 \cdot \mathbf{d}_{g,p}^1 (C_{kp}^{-1} - D_{kp}^{-1}) \right] \chi(\tau_g, \tau_e), \quad (40)$$

where the $n \times n$ matrices \mathbf{C} and \mathbf{D} and the vector Γ are respectively defined as

$$\mathbf{C} = \mathbf{B} - \mathbf{A}, \quad (41)$$

$$\mathbf{D} = \mathbf{B} + \mathbf{A}, \quad (42)$$

$$\Gamma = \mathbf{S}^T \mathbf{E} \mathbf{K}, \quad (43)$$

and where

$$\chi(\tau_g, \tau_e) = \sqrt{\frac{\det \mathbf{a}_g \det \mathbf{a}_e}{\det \mathbf{C} \det \mathbf{D}}} e^{\frac{i}{\hbar} (\mathbf{K}^T \mathbf{E} \mathbf{K} - \Gamma^T \mathbf{C}^{-1} \Gamma)} e^{-i\omega_{ge} \tau_e}. \quad (44)$$

Note that the matrices \mathbf{A} , \mathbf{B} and \mathbf{E} , hence \mathbf{C} , \mathbf{D} and Γ , all depend on the parameters τ_g and τ_e through the definitions of \mathbf{a}_g , \mathbf{a}_e , \mathbf{b}_g and \mathbf{b}_e [Eqs. (31) and (32)]. The short time $t \rightarrow 0$ of the correlation function, $C_{ge}(0, -i\beta_{\text{eff}}\hbar)$, reduces to

$$\frac{1}{Z_e(T_{\text{eff}})} C_{ge}(0, -i\beta_{\text{eff}}\hbar) = |\mathbf{d}_e^0|^2 + \sum_k \frac{\hbar}{2\omega_{e,k}} |\mathbf{d}_{e,k}^1|^2 \coth(\beta_{\text{eff}}\hbar\omega_{e,k}), \quad (45)$$

which simply corresponds to the average of the squared transition dipole moment at temperature T_{eff} in the electronic excited state. This was expected from the definition of the correlation function in Eq. (15). From Eq. (45), the correlation function controlling the emission spectrum contains two sets of contributions: the Franck-Condon contribution given by the transition dipole moment at the electronic excited state equilibrium geometry and the HT contributions arising from each normal mode. The FC contribution can be determined from the oscillator strength f_e^{FC} , defined here as

$$f_e^{\text{FC}} = \frac{2m_e}{3\hbar e^2} \omega_{ge} |\mathbf{d}_e^0|^2. \quad (46)$$

The temperature-dependent HT contribution f_e^{HT} is obtained from the corresponding oscillator strength

$$f_e^{\text{HT}}(T_{\text{eff}}) = \sum_k f_{e,k}^{\text{HT}}(T_{\text{eff}}) = \sum_k \frac{m_e \omega_{ge}}{3e^2 \omega_{e,k}} |\mathbf{d}_{e,k}^1|^2 \coth(\beta_{\text{eff}}\hbar\omega_{e,k}). \quad (47)$$

Note that when the electronic transition is forbidden by symmetry, the transition dipole moment at the equilibrium geometry vanishes ($\mathbf{d}_e^0 = \mathbf{0}$). However, in general the normal mode contribution will not vanish for any ungerade mode that breaks the inversion symmetry of the molecule, even at vanishing temperature, due to the delocalized nature of the wavefunction around the equilibrium position.

C. Computational details

The calculation of the RF rate constants, PE and absorption spectra through Eqs. (14), (17), (18) and (40) requires the knowledge of the optimized geometries, normal mode coordinates and harmonic frequencies in the electronic ground and excited states as well as the transition dipole moment between the electronic ground and excited states and its derivatives computed at the electronic ground or excited state geometries [Eqs. (24) and (25)]. All these parameters were obtained using quantum chemistry calculations. In the past, a large number of studies conducted at various theoretical levels have been devoted to the description of PAHs electronic excited states.^{36,39–49} For low-lying electronic excited states, time-dependent density-functional theory (TD-DFT)^{50,51} has been shown to give reliable results for PAHs with various charge states.^{36,48,49}

The structure and properties of the electronic ground state denoted as S_0 and D_0 for the neutral and cationic molecules, respectively, were obtained using density-functional theory (DFT) calculations with the ω B97xD functional⁵² combined with the cc-pVTZ basis set.^{53,54} Electronic excited states properties of cations were determined using TD-DFT at the same level of theory as for the electronic ground states. The same functional and basis set were used recently to describe RF fluorescence in naphthalene and azulene.¹⁷ All electronic structure calculations were performed using the Gaussian16 quantum chemistry package.⁵⁵

In the calculation of the transition dipole moment between the electronic ground and excited states through Eq. (25), the electronic excited state minimum geometry was used. Alternatively, and as argued by Baiardi and coworkers,³⁵ the electronic ground state minimum geometry can also be employed for the same purpose, which is a way to assess the validity of the linear approximation. Such calculations were carried out for Np^+ in the D_1 and D_2 states. To compare the transition dipole moments determined using the electronic ground and excited state geometries, the dimensionless quantity ε was calculated as

$$\varepsilon = \frac{\sum_{k=1}^n \left| \mathbf{d}_{e,k}^1(\mathbf{r}_e) - \mathbf{d}_{e,k}^1(\mathbf{r}_g) \right|^2}{\sum_{k=1}^n \left| \mathbf{d}_{e,k}^1(\mathbf{r}_e) \right|^2} \quad (48)$$

In the case of the D_2 state, very small variations in the transition dipole moment between the electronic ground state geometry and the electronic excited state geometry are obtained, with $\varepsilon = 4\%$. In contrast, for the D_1 state, the variations are more pronounced with $\varepsilon = 23\%$. Nevertheless, and while the results presented below may quantitatively depend on the choice of reference, the qualitative conclusions should generally hold.

Microcanonical properties depend on the density of vibrational modes in the various electronic states. Within the harmonic approximation, the densities of vibrational states were computed using the Stein-Rabinovitch counting algorithm,⁵⁶ which is more accurate than the Beyer-Swinehart method⁵⁷ and does not introduce rounding errors to the mode energies. An energy bin of $\Delta E = 100 \text{ cm}^{-1}$ was employed. The time correlation functions of Eq. (40) were computed on a regular time grid of 100000 points with a timestep of 0.167 fs and the various spectra defined by Eqs. (14), (17) and (18) were determined using fast Fourier transform with a 20 cm^{-1} resolution. In practice, to impose a vanishing time-correlation function at long time scales, the time correlation functions were multiplied by a Gaussian function of fixed width, resulting in a convoluted spectrum. Gaussian functions with full width at half maximum (FWHM) of 400 cm^{-1} for IR absorption, and 50 cm^{-1} for the PE and RF spectra, were used, respectively.

III. RESULTS

A. Electronic structure of the cations

For all Np^+ , An^+ , and Py^+ cations, the two lowest electronic excited states D_1 and D_2 were considered in the analysis. For the pyrene cation, D_3 was also included due to its energetic proximity with D_2 . For each electronic excited state, the geometry was locally optimized, starting from the electronic ground state equilibrium configuration. After optimization, the D_{2h} point group is preserved in all electronic excited states. Table I lists the main energetic features of the various electronic excited states, namely their adiabatic relative energy with respect to the neutral molecule in the electronic ground state, and the transition energy between the vibrational ground state of the electronic states of the cation relative to the ground vibrational and electronic ground state of the neutral molecule. This energy includes the zero-point contribution in the harmonic approximation and can be directly compared to photoelectron spectroscopy measurements, in particular with the location of the origin band.^{39–41,58,59} Our quantum chemical results are very similar to earlier TD-DFT calculations.^{44–46} Compared to experimental values, the error on the position of the cationic electronic states with respect to the neutral electronic ground state ranges from 0.01 eV (D_1 state of Py^+) to 0.31 eV (D_0 state of An^+), and it is noteworthy that the largest errors occur for the electronic ground states. Overall, our calculations tend to underestimate the transition energies with respect to experimental data, except for the D_3 state of Py^+ which is slightly overestimated.

Molecule	State	relative energy (eV)	transition energy (eV)		$f_e^{\text{FC}}(\times 10^3)$	$f_e^{\text{HT}}(\times 10^3)$	
			calc.	exp.		0 K	2000 K
Np	$S_0 (X^1A_g)$	0	0	0	–	–	–
	$D_0 (X^2A_u)$	7.92	7.91	8.15 ^a	–	–	–
Np^+	$D_1 (A^2B_{3u})$	8.74	8.76	8.88 ^a	×	0.6596	0.9503
	$D_2 (B^2B_{2g})$	9.81	9.79	10.08 ^a	82.12	0.7252	1.926
An	$S_0 (X^1A_g)$	0	0	0	–	–	–
	$D_0 (X^2B_{2g})$	7.15	7.16	7.47 ^b	–	–	–
An^+	$D_1 (A^2B_{1g})$	8.53	8.52	8.57 ^b	×	4.745	7.641
	$D_2 (B^2A_u)$	9.03	9.05	9.23 ^b	164.0	1.113	1.571
Py	$S_0 (X^1A_g)$	0	0	0	–	–	–
	$D_0 (X^2B_{1g})$	7.19	7.19	7.41 ^c	–	–	–
Py^+	$D_1 (A^2B_{2g})$	8.25	8.26	8.26 ^c	×	1.243	1.817
	$D_2 (B^2B_{3u})$	8.94	8.93	9.00 ^c	34.34	4.565	10.07
	$D_3 (C^2A_u)$	9.32	9.35	9.29 ^c	58.67	15.43	18.44

^a Ref. 41, ^b Refs. 39 and 58, ^c Refs. 40 and 59

TABLE I. Spectroscopic notation, relative energy, transition energy and transition dipole moment contributions of the various electronic states considered in this study. The symbol \times is used to indicate a symmetry-forbidden transition.

In order to evaluate the quality of the potential energy surfaces in the electronic ground and excited states with the present (TD-)DFT methods, the theoretical PE spectra were determined for the three cations using Eq. (18). To refine the model further, the positions of the electronic states were also shifted to better match the experimental transition energies obtained from Ref. 41 for Np^+ , from Refs. 39 and 58 for An^+ , and from Refs. 40 and 59 for Py^+ . In the following, these shifts are used to identify the spectral positions of the various electronic states, in particular when computing the RF rate constants.

Fig. 3a) shows the harmonic theoretical PE spectra for Np^+ , including the contributions from states D_0 , D_1 and D_2 and assuming that the system initially resides in the vibrational ground state of the neutral molecule. The theoretical spectrum of the D_0 state shows a clear vibrational progression with an origin band located at 8.15 eV and additional bands at 8.33 eV and 8.52 eV,

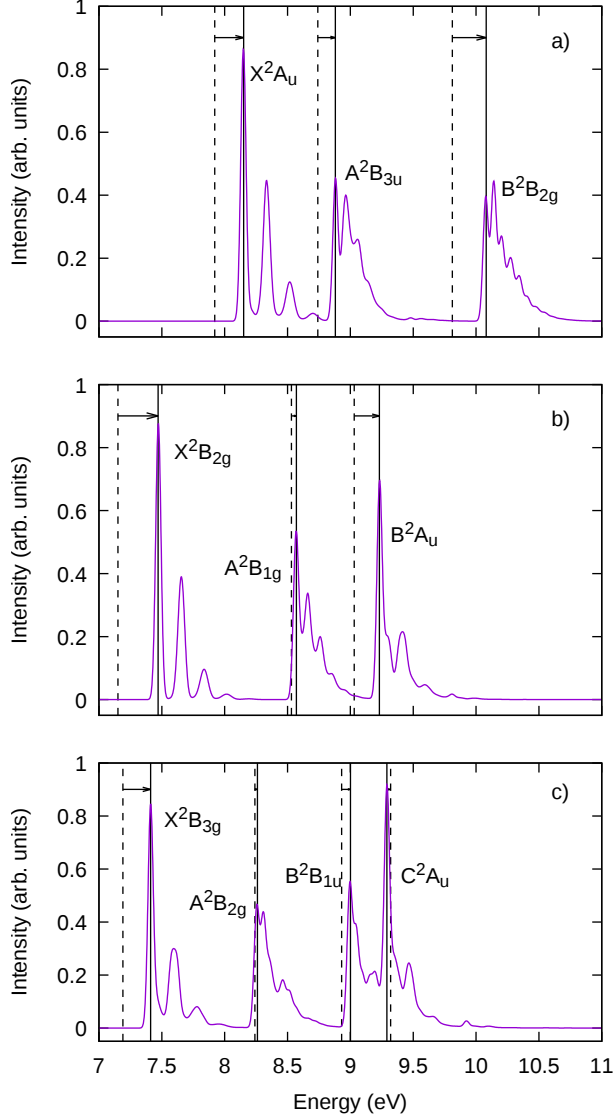


FIG. 3. Simulated photoelectron spectra for (a) Np^+ ; (b) An^+ ; and (c) Py^+ . The spectra are shifted horizontally to match experimental lines. The original positions of the states, calculated by our model, are shown by dashed vertical lines, while the full lines show the shifted positions. All spectra are convoluted with a Gaussian with FWHM of 50 cm^{-1} .

corresponding to a vibrational frequency of 1480 cm^{-1} . This is comparable to the experimental spectrum from Mayer and coworkers,⁶⁰ where a similar vibrational progression with frequency of 1408 cm^{-1} was reported. In the case of the states D_1 and D_2 , the PE spectrum of Np^+ is broader and without a clear vibrational progression, also in agreement with the measurements.⁴¹

Figs. 3b) and 3c) show the corresponding PE spectra for An^+ and Py^+ , respectively. Similarly as for Np^+ , clear vibrational progressions are also seen in the D_0 states of both An^+ and

Py^+ cations. In the anthracene case, the bands found at 7.47 eV, 7.65 eV, and 7.84 eV correspond to a vibrational frequency of about 1500 cm^{-1} , comparable with the experimental PE spectra of Boschi and coworkers, within 100 cm^{-1} residual error.⁵⁸ In the case of Py^+ , the bands located at 7.41 eV, 7.60 eV, and 7.78 eV correspond to a vibrational frequency of 1490 cm^{-1} , in satisfactory agreement with the values of 1390 cm^{-1} measured by Boschi and Schmidt⁵⁹ and 1450 cm^{-1} according to Vala and coworkers.⁴⁰ Relative to Np^+ , the electronic excited states spectra of the two other cations exhibit broader peaks, without a clear progression and in agreement with experiments.^{39,40,58,59}

Besides energetic properties, Table I also provides the FC and the HT contributions to the oscillator strength involved in Eqs. (46) and (47), between the electronic ground and excited states of the cations. The various oscillator strengths were determined using the theoretical adiabatic transition energies. The HT contribution was calculated at 0 K, and at a more realistic effective temperature of 2000 K that corresponds to about 5 eV lying in the electronic ground state of Np^+ (vide infra). Our calculated FC oscillator strengths are of similar magnitude compared to previously published work, although consistently higher. For example, in the case of the D_2 state of Np^+ , our calculated value of 0.082 is larger than the value of 0.047 reported by Malloci and coworkers⁴⁵ based on DFT/B3LYP/4-31G, as well as the value of 0.057 given by Hirata and coworkers⁴⁴ based on DFT/BLYP/6-31G** together with the Tamm–Dancoff approximation. However, our total oscillator strength (FC plus HT) for the D_2 state of Np^+ at zero effective temperature compares well with the value of 0.09 given by Lee and coworkers based on the DFT/LC- ω HPBE/cc-pVTZ method.¹⁷

Except for symmetry-forbidden transitions, the FC contribution is found to be dominant compared to the HT contribution for all states and all cations considered. However, the HT contribution becomes non negligible in some cases, especially for Py^+ where it can amount to more than a fifth of the total oscillator strength. For all states, the HT contribution increases with increasing effective temperature. Such an increase varies in magnitude depending on the cation and electronic state, and can be relatively minor (18% for the D_3 state of Py^+) or conversely quite strong (166% for the D_2 state of Np^+). These variations arise from differences in the transition dipole moment surface. Specifically, electronic excited states where the transition dipole moment varies the most with low-frequency vibrational modes are found to exhibit the largest increase as a function of the effective temperature. For the D_1 states, which are forbidden by symmetry, the HT contribution to the oscillator strength does not vanish but remains small compared to the FC oscillator strength of

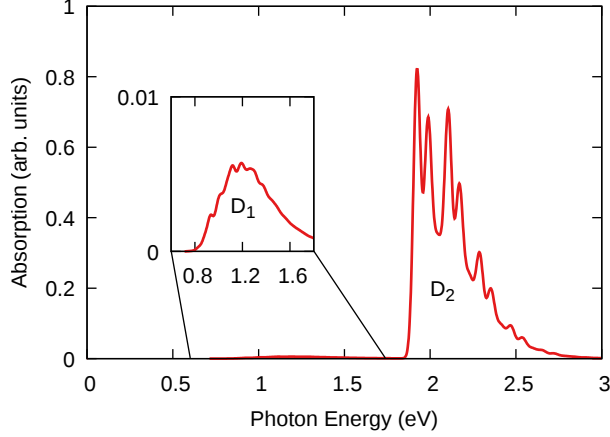


FIG. 4. Simulated absorption spectrum for Np^+ at zero temperature, convoluted using a Gaussian function with FWHM of 400 cm^{-1} . The inset highlights the $0.6\text{--}1.8 \text{ eV}$ energy range.

symmetry-allowed states. For instance, in the case of Np^+ , the total oscillator strength for the D_1 state is about a hundred times weaker than that of the D_2 state. Such a difference is illustrated in Fig. 4, showing the simulated absorption spectrum for Np^+ obtained using Eq. (17) and assuming a 0 K equilibrium temperature, the individual peaks being convoluted with a 400 cm^{-1} Gaussian function for a better comparison with the experimental spectrum of Bally and coworkers.⁴¹

The theoretical absorption spectrum displays a strong band corresponding to the D_2 state, with a clear vibrational progression also seen in the experimental spectrum.⁴¹ A very weak absorption band is also found, corresponding to the D_1 state, with an intensity more than two orders of magnitude weaker than the D_2 band. This ratio is in accordance with the ratio between the transition dipole moments of the two states, as given in Table I. Such a weak signal is also consistent with experimental measurements,⁴¹ in which no contribution from the D_1 state was reported — the D_1 contribution being thus likely hidden in the noise.

The overall HT oscillator strength can be decomposed over the various normal modes. This decomposition is illustrated in Fig. 5, where the HT oscillator strength $f_{e,k}^{\text{HT}}$ from each normal mode for the symmetry-forbidden D_1 states of Np^+ , An^+ and Py^+ at $T = 2000 \text{ K}$ is obtained from Eq. (47). For all molecules, as expected, only the ungerade normal modes that break the inversion symmetry produce a transition dipole moment. Fig. 5 shows that the high-frequency CH stretching region only gives a negligible contribution to the transition dipole moments and that the normal modes contributing the most to the oscillator strength are of B_{1u} and B_{2u} symmetries. In particular, for Np^+ , the two modes having the highest contribution are both of B_{1u} symmetry

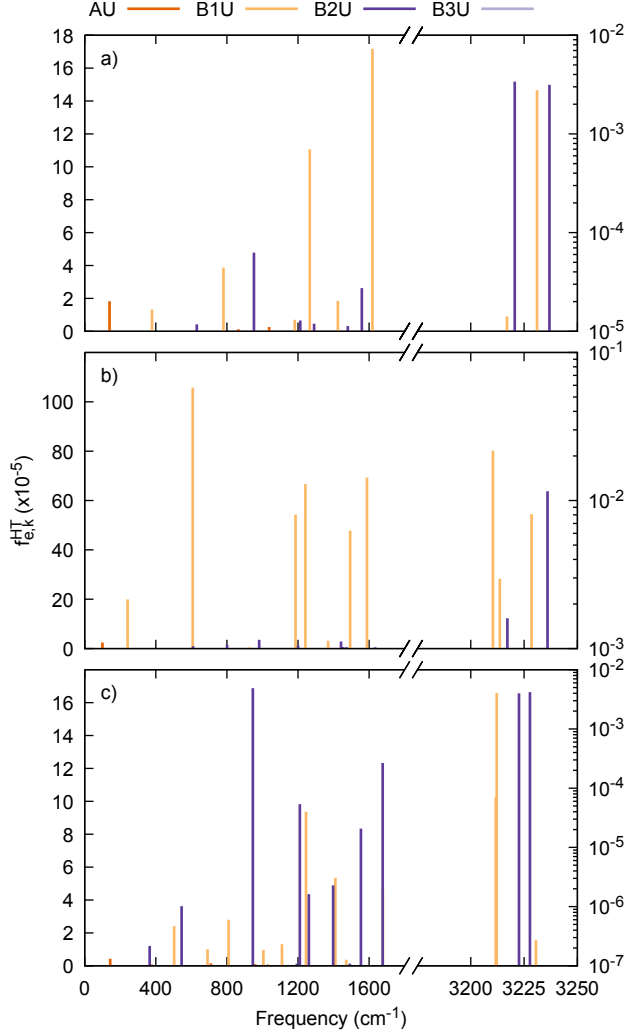


FIG. 5. Mode-specific Herzberg-Teller oscillator strength $f_{e,k}^{HT}(T)$ for the D_1 state of the cations (a) Np^+ ; (b) An^+ ; and (c) Py^+ , at $T = 2000$ K and as a function of the harmonic frequency $\omega_{e,k}$. The gerade vibrational modes have no contribution. The oscillator strengths in the CH stretching region are given in logarithmic scale for better visualization.

with frequencies 1618.9 cm^{-1} and 1266.2 cm^{-1} . These two modes correspond to combinations of CC stretching and CH in-plane bending motions. In the case of An^+ , the strongest contributing mode is a B_{1u} mode with frequency 607.7 cm^{-1} corresponding mostly to collective CC stretching motion. For Py^+ , the main contribution arises from a B_{2u} mode with frequency 946.0 cm^{-1} also corresponding to a collective CC stretching motion. For the three cations, a small contribution from a completely antisymmetric A_u vibrational mode is also noticed in the very low frequency range (139.7 cm^{-1} , 99.6 cm^{-1} and 143.3 cm^{-1} for Np^+ , An^+ and Py^+ , respectively).

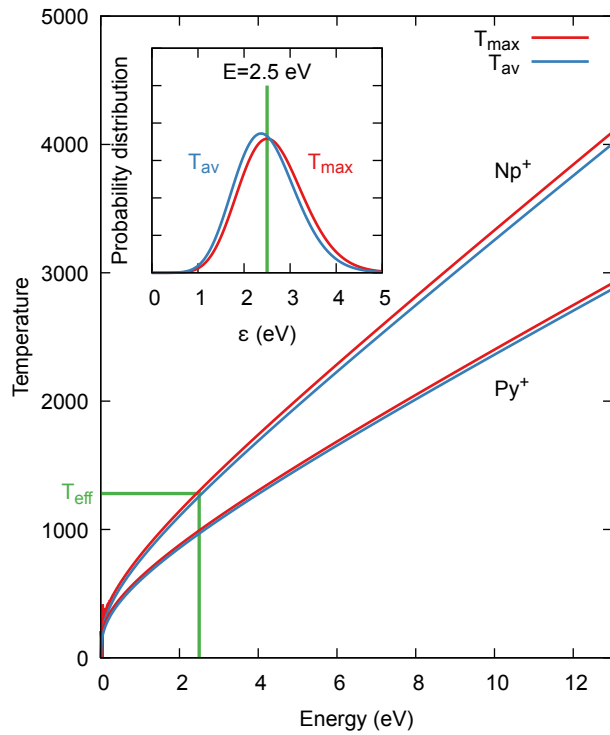


FIG. 6. Average temperature T_{av} and maximum temperature $T_{max} = T_{\mu}$ as a function of the microcanonical energy for the D_0 states of Np^+ and Py^+ . The inset shows the canonical probability distributions of internal energies for the D_0 state of Np^+ obtained with T_{av} and T_{max} as effective temperatures at 2.5 eV microcanonical energy.

Our model, which quantifies the effect of molecular deformation on the electronic transition dipole moment, relies on the linear expansion of the transition dipole moment [Eqs. (24) and (25)] and the harmonic approximation. Appendix C shows that both assumptions are well satisfied for the present systems under the operating conditions of internal energies lower than 13.6 eV.

B. Effective canonical temperature

In our model, Eq. (11) is solved by replacing the original microcanonical statistical distribution by an equivalent canonical distribution at an effective temperature T_{eff} . Two possible choices for T_{eff} in this approximation are based on adjusting either the maximum (T_{max}) or the average (T_{av}) of the canonical distribution to match the microcanonical energy E_0 . These choices are illustrated in the inset of Fig. 6, where the canonical probability distributions in the D_0 state of Np^+ evaluated with the two temperatures T_{max} and T_{av} and corresponding to 2.5 eV microcanonical energy, are

shown as a function of internal energy. For this harmonic system, and for any electronic state i , the average energy $\langle E \rangle$ from which the effective temperature T_{av} is obtained is an explicit function of the normal mode frequencies,

$$\langle E \rangle(T) = \sum_{k=1}^n \frac{\hbar\omega_{i,k}}{e^{\beta\hbar\omega_{i,k}} - 1}. \quad (49)$$

For T_{max} , the peak of the probability distribution is, by definition, precisely centered at the microcanonical energy, while for T_{av} the corresponding peak is slightly shifted towards lower energies. This is a direct result of the asymmetry of the Boltzmann distribution. Fig. 6 also shows the energy versus temperature variations for both the microcanonical ($T_{\text{max}} = T_{\mu}$) and the canonical (T_{av}) temperatures in the case of the D_0 state of Np^+ and in the case of the D_0 state of Py^+ . As expected for an harmonic system, both temperatures increase linearly at high energies, but with slightly different slopes. As a result, the canonical temperature is somehow slightly lower than the microcanonical temperature. The difference between the two temperatures is directly related to the finite size of the system, and illustrates that the two statistical ensembles are equivalent only in the thermodynamic limit. This can be seen in the main Fig. 6 which compares the two choices of effective canonical temperatures for Np^+ and Py^+ . In Fig. 6, the canonical temperature is a well-defined, monotonic and therefore bijective function of energy. However, such is not the case for the microcanonical temperature which is only defined for energies that are large enough for the density of states to be approximated by a continuous and differentiable function. This can be seen as a cusp appearing at low energy in the microcanonical temperature represented in Fig. 6.

In addition to the effective temperature, the probability $P_n^k(E_0)$ to find n quanta in mode k at internal energy E_0 was determined in the original microcanonical ensemble, as well as in the canonical ensembles using either T_{max} or T_{av} as the effective canonical temperature. In the microcanonical ensemble, and for any electronic state i , the probability $P_n^k(E_0)$ is defined by

$$P_n^k(E_0) = \frac{\Omega_i^{(k)}(E - n\omega_k)}{\Omega_i(E_0)}, \quad (50)$$

where $\Omega_i^{(k)}$ is the vibrational density of states excluding the vibrational mode k . In the canonical ensemble, this probability is given by

$$P_n^k(T_{\text{eff}}) = e^{-n\beta_{\text{eff}}\omega_{i,k}} \left(1 - e^{-\beta_{\text{eff}}\omega_{i,k}}\right). \quad (51)$$

The variations of this quantity with increasing number of quanta are shown in Figs. 7a) and 7b) for the lowest-frequency ($\omega_k = 155.4 \text{ cm}^{-1}$) and the highest-frequency ($\omega_k = 3239.1 \text{ cm}^{-1}$) modes of

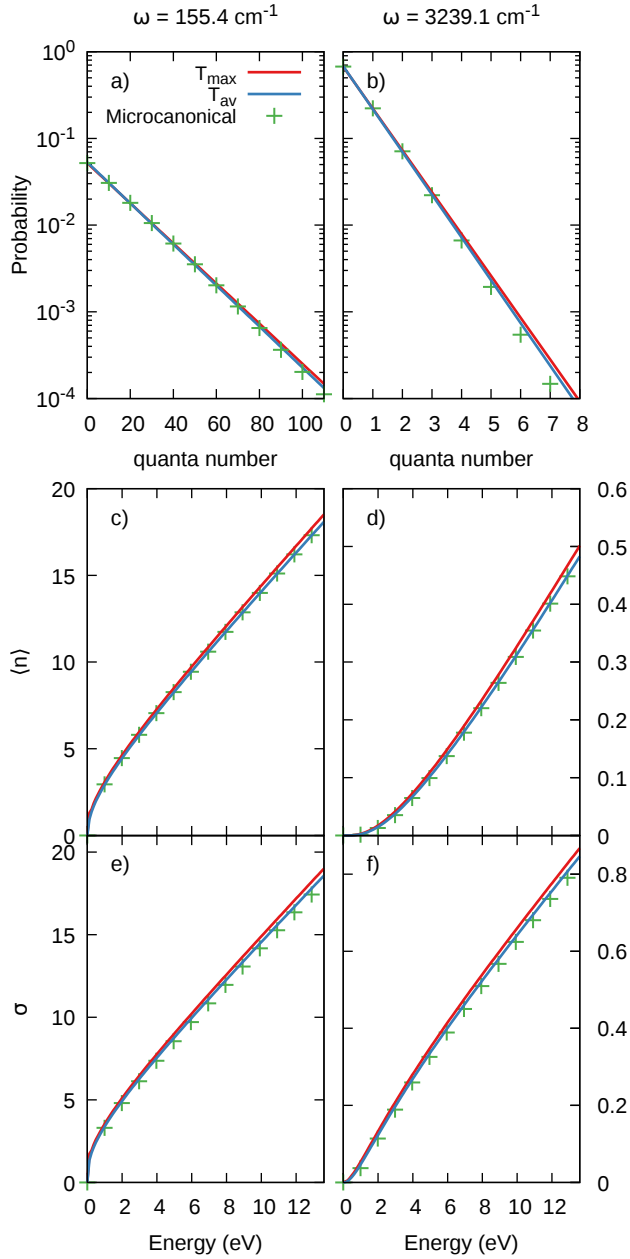


FIG. 7. Statistics of the naphthalene cation being in specific vibrational modes as a function of internal energy, from the true microcanonical ensemble, compared with the predictions in the canonical ensemble with effective temperatures taken as T_{\max} or T_{av} , as defined in the text. (a,b) Probability of being in the mode; (c,d) average numbers of quanta; (e,f) mean-square fluctuation around the average numbers. (a,c,e) Lowest-frequency mode with $\omega = 155.4 \text{ cm}^{-1}$; (b,d,f) Highest-frequency mode with $\omega = 3239.1 \text{ cm}^{-1}$.

the D_0 state of Np^+ and at the highest energy considered in this work, $E_0 = 13.6$ eV. As expected, this probability decreases exponentially when described in the canonical ensemble, whatever the underlying choice for the corresponding temperature between T_{\max} and T_{av} . In contrast, the true microcanonical probability decreases exponentially for small values of n but deviates from this behavior at larger n . Overall, the differences between the various probabilities are small but the canonical temperature value T_{av} that originates from matching E_0 to $\langle E \rangle$ provides the best agreement to the microcanonical reference. This happens to hold for all values of the internal energy and for all vibrational modes, as evaluated from the statistics in the number of quanta n_k as a function of internal energy E . Figs. 7c) and 7d) show the variations of the average numbers $\langle n_k \rangle$ for the lowest- and highest-frequency modes of Np^+ at 155.4 cm^{-1} and 3239.1 cm^{-1} , respectively, while Figs. 7e) and 7f) display the mean square fluctuations $\sigma_k(E)$ associated with the corresponding distributions.

For both modes, the average number of quanta calculated in the canonical ensemble employing temperature T_{av} is almost identical to the reference value obtained in the microcanonical ensemble. This result was expected since the canonical temperature is defined through the average number of quanta. By looking at the deviation, residual differences between the distributions appear but the canonical temperature T_{av} is consistently a better choice compared to the alternative choice $T_{\max} = T_{\mu}$ of the true microcanonical temperature. Such conclusions also hold for the other cationic PAH and different electronic states considered in this work (results not shown). This justifies our choice of the canonical ensemble with effective temperature $T_{\text{eff}} = T_{\text{av}}$ when modeling the RF differential rate constants.

C. RF rate constants

Having validated the canonical framework for computing the RF rate constants through Eq. (14) with the temperature T_{av} serving as the effective canonical temperature, Fig. 8 shows the variations of the total rate constants [see Eq. (16)] for the three cations, highlighting the various contributions from individual electronic states. As was the case for the PE spectra, the positions of the electronic excited states were shifted to better match experimental data. These shifts are essential in determining the occupation probabilities of the various electronic excited states.

While the symmetry-forbidden D_1 state contributes negligibly compared to symmetry-allowed states in the absorption spectrum, it can make a comparable or even dominant contribution to the

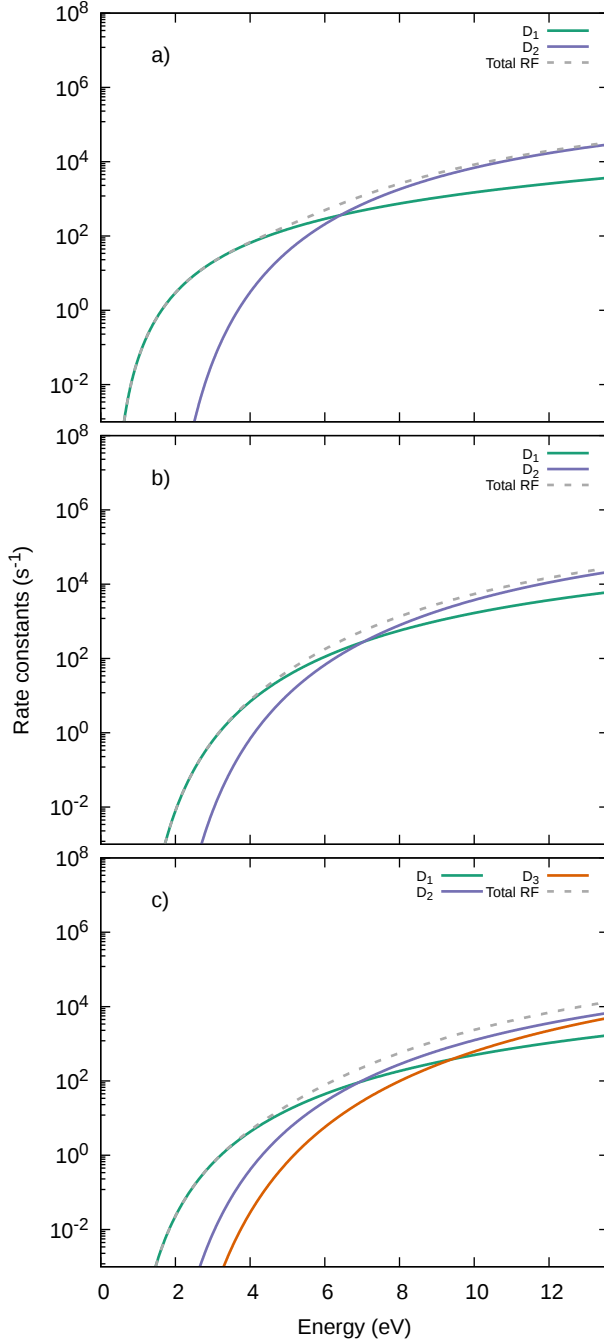


FIG. 8. State-resolved (solid lines) and cumulated (dashed lines) recurrent fluorescence rate constants for (a) Np^+ , (b) An^+ , and (c) Py^+ , as a function of internal energy.

RF emission spectrum depending on internal energy. For Np^+ , at energies below the threshold of the D_2 state (1.93 eV), the D_1 state is obviously dominant, being the only state that can contribute. However, above the D_2 state threshold, D_1 remains dominant until the internal energy reaches $E = 6.41$ eV. Despite its very low oscillator strength, the significant contribution of the D_1 state arises

from its much lower adiabatic energy, which leads to a stronger population in the D_1 state and compensates for the weak transition dipole moment. At higher energies, the D_2 state eventually dominates the total RF rate constant, contributing up to 7.45 times more than the D_1 state at $E = 13$ eV.

In the case of the An^+ and Pyr^+ cations, similar trends arise. For An^+ , the D_1 state prevails over the D_2 state up to $E = 7.04$ eV and, at $E = 13$ eV, its contribution is only 3.33 times weaker than that of the D_2 state. For Pyr^+ , the D_1 state emission exceeds that of D_2 for energies below $E = 6.91$ eV, and that of D_3 for energies below $E = 9.39$ eV.

In Fig. 9, the normalized differential rate constants for Np^+ , $k^{\text{RF}}(\omega; E)/k_{\text{tot}}^{\text{RF}}(E)$, are represented as a function of the emitted photon frequency and for internal energies in the 4–8 eV range. The contributions from both electronic excited states are shown separately, highlighting the decreasing importance of the D_1 state, relative to D_2 , as energy is increased. This is also in accordance with the conclusions from Fig. 8. Across all displayed energies, the differential rate constant shows a double peak behavior that indicates the separate contributions from the two electronic excited states. For each band, the emission spectrum is broad and lacks vibrational structure, which is directly attributable to the high excess energy in the molecule, resulting into a large number of vibrational quanta distributed over many modes. The linewidths of both the D_1 and D_2 bands increase with increasing energy, also due to the larger number of vibrational quanta. The D_1 band exhibits a FWHM of 4860 cm^{-1} at $E = 4$ eV and 6220 cm^{-1} at $E = 8$ eV. For the D_2 band, the FWHM is 4520 cm^{-1} at $E = 4$ eV and 6280 cm^{-1} at $E = 8$ eV. While the position of the maximum of the D_2 band remains nearly constant around $\omega = 13600 \text{ cm}^{-1}$, the maximum of the D_1 band shifts significantly from 5120 cm^{-1} to 6560 cm^{-1} . This behavior originates from the ω^3 term in the expression of the rate constant [see Eq. (14)], which favors higher frequencies. Since the D_1 band is relatively low in energy, it is particularly sensitive to this term, causing the peak of the differential rate constant to shift toward higher frequencies. In contrast, the D_2 band, being higher in energy, is only barely affected by this effect.

The variations of the normalized differential rate constants for An^+ are shown in Fig. 9 as well. As is the case for Np^+ , the contributions from the two bands D_1 and D_2 are also clearly seen. Because the D_1 state is located at a higher energy, it only shifts from $\omega = 6760 \text{ cm}^{-1}$ at 4 eV to 7500 cm^{-1} at 8 eV. At the low energy $E = 4$ eV, the D_2 band exhibits a small vibrational structure with two peaks located at $\omega = 12560 \text{ cm}^{-1}$ and 13820 cm^{-1} . This vibrational feature disappears at higher energies and the band is located at $\omega = 12780 \text{ cm}^{-1}$ at $E = 8$ eV.

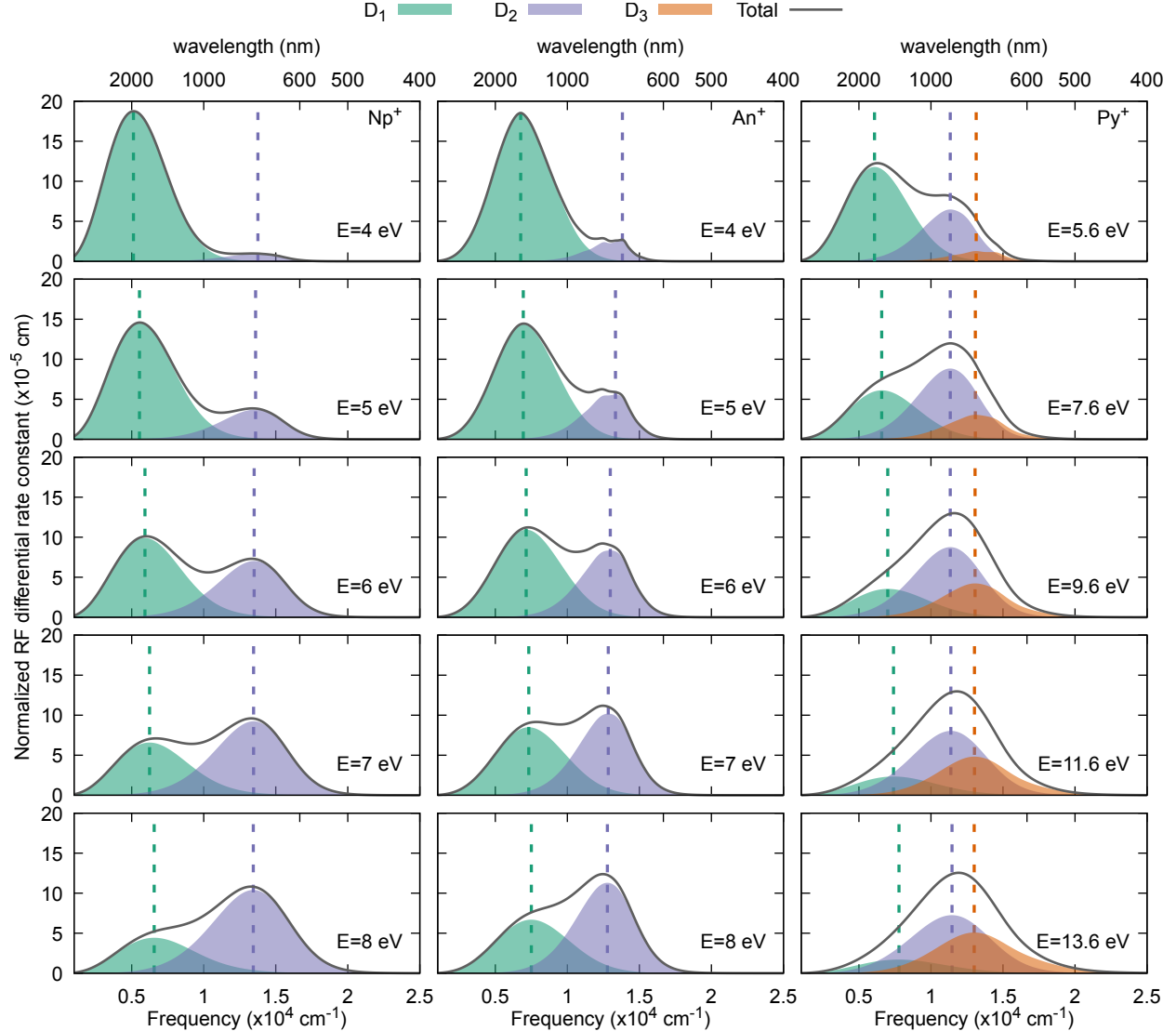


FIG. 9. Normalized RF differential rate constants for Np^+ (left panels), An^+ (middle panels) and Py^+ (right panels) as a function of the photon frequency ω and for various internal energies, highlighting the contributions from the D_1 , D_2 and D_3 electronic states.

The corresponding rate constants for the pyrene cation, also represented in Fig 9, now highlight the contribution from the D_3 state, in addition to the lower D_1 and D_2 states. At low energy, the total emission spectrum exhibits a double-peak structure corresponding to these latter bands. As the energy increases, the energy of the D_1 band located near 7000 cm^{-1} weakens while the D_2 band located at $\omega = 11400 \text{ cm}^{-1}$ becomes stronger. At very high energy, the contribution of the D_3 state located around 13200 cm^{-1} equals the contribution of the D_2 band, producing a single broad peak around 12000 cm^{-1} .

D. Experimental comparison

Saito and coworkers measured the RF emission spectrum of Np^+ using various bandpass filters.¹⁰ In this experimental work, the cations were excited at an average internal energy of approximately 6.5 eV. The spectrum recorded by these authors initially increases around 560 nm ($\sim 17,900 \text{ cm}^{-1}$), reaches a maximum between 670—700 nm ($\sim 14,900\text{--}14,300 \text{ cm}^{-1}$) and finally decreases slightly at photon energies of about 850 nm ($\sim 11,800 \text{ cm}^{-1}$). Comparing with the absorption spectrum experimentally measured for Np^+ by Bally and coworkers,⁴¹ the RF emission spectrum reported by Saito and coworkers agrees in the increasing region from 560 to 700 nm but shows a marked difference at higher wavelengths where the absorption spectrum vanishes. As shown in Fig. 9a, the position of the D_1 state is too low to be clearly resolved with the bandpass filters used in Ref. 10. However, our calculations also suggest that the slight decrease observed in the 700—850 nm region can be explained by the broad width of the D_2 band, likely with a contribution from the D_1 state.

More recently, Kusuda and coworkers¹¹ measured the RF emission spectrum of An^+ with a similar experiment as for Np^+ . The average internal energy in the cations was around 6 eV. In Ref. 11, the measured RF emission spectrum steadily increases from 625 nm and reaches a maximum at 775 nm, before remaining almost constant until the measured wavelength reaches its maximum at 825 nm. In contrast with the Np^+ experiment,¹⁰ the position of the maximum of the RF emission spectrum is observed at a lower frequency than the absorption spectrum. As shown in Fig. 9b, our calculations clearly suggest that the width of the D_2 band cannot explain the signal measured in the 800 nm region alone. However, a strong additional contribution from the D_1 state suffices to solve this discrepancy and account for the different behaviors of the naphthalene and anthracene cations.

IV. CONCLUSIONS AND PERSPECTIVES

Recurrent fluorescence is a crucial relaxation mechanism that enhances the stability of polycyclic aromatic hydrocarbons and other molecular systems in the interstellar medium. In this work, a novel statistical model was introduced to describe RF rate constants, explicitly incorporating Herzberg–Teller and Duschinsky rotation effects, as well as a full account of vibrational progressions within the harmonic approximation. Being aimed at isolated molecules, the model is intrin-

sically built on microcanonical statistics. However, a canonical framework was found to be more effective and even quantitative, provided that the temperature is chosen so the microcanonical energy matches the internal energy in the canonical ensemble.

Application of the model requires ingredients that can be obtained from quantum chemistry calculations, here based on density-functional theory in its static and time-dependent versions for the highly symmetric naphthalene, anthracene, and pyrene cations. Our study demonstrates that, for these systems, the low-lying, symmetry-forbidden electronic excited states may contribute more significantly to their cooling efficiency than higher-energy, symmetry-allowed states, particularly for energies typically below 6.5 eV. This energy range is of particular interest because, above this threshold, fragmentation likely dominates the relaxation cascade, whereas below approximately 5 eV, infrared photon emission is the primary relaxation pathway.¹⁷ This range of interest precisely corresponds to the typical energies probed in experiments using ion traps or storage rings, such as those conducted by Saito and coworkers¹⁰ on the naphthalene and anthracene cations.

Our simulated spectra suggest that the photons emitted in the long-wavelength range, as recorded in the experiment of Ref. 10, likely originate from these low-lying forbidden states. Therefore, our findings not only advance the understanding of PAH relaxation kinetics in laboratory settings but also emphasize the critical role of forbidden transitions in PAH survival under actual astrochemical environments.

Future efforts will be aimed at extending the model to quantify the impact of low-lying forbidden states on the relaxation cascade of various PAHs. Such extensions require explicitly accounting for competing relaxation processes, including infrared emission, fragmentation, as well as isomerization. Because some of these processes are intrinsically anharmonic, it would be useful to extend the present model beyond the harmonic approximation, either through perturbative expansions or molecular dynamics simulations, ideally corrected for nuclear quantum effects.

At present, the model has been solely used to describe recurrent fluorescence from an electronic excited state back to the electronic ground state. In a straightforward extension, the contribution of recurrent fluorescence between two electronic excited states could be also considered. Additionally, the contribution of inverse fluorescence, a process involving fluorescence from a vibrationally excited electronic ground state to an electronic excited state, could be quantified as well. Despite being mentioned as a possible mechanism by Léger and coworkers several decades ago,⁵ this contribution, though expectedly small, remains to be quantitatively assessed.

Appendix A: Generalization to multiple electronic states

Generalization to the case of many electronic states within the Born-Oppenheimer approximation is straightforward, as long as all electronic states are uncoupled. The total RF differential rate constants are thus expressed as the sum over all electronic excited states as

$$k^{\text{RF}}(\omega; E) = \sum_{i \neq g} \frac{\omega^3}{3\pi\varepsilon_0\hbar c^3} P_i(E) \int_{-\infty}^{+\infty} \frac{dt}{2\pi} \frac{1}{Z_i(T_{\text{eff}})} C_{gi}(-t, t - i\beta_{\text{eff}}\hbar) e^{i\omega t}, \quad (\text{A1})$$

where $P_i(E)$ is now defined by the ratio of microcanonical densities of states:

$$P_i(E) = \frac{\Omega_i(E)}{\sum_j \Omega_j(E)}. \quad (\text{A2})$$

In the case of multiple electronic states, the various time correlation functions $C_{gi}(\tau_g, \tau_e)$ are determined separately and summed together, each function being weighted by the appropriate probability $P_i(E)$. Note that in the case of both absorption and PE spectra, and since the initial electronic state is always the ground state, the total spectra correspond to the direct sums of the relevant correlation functions for each electronic state.

Appendix B: Expression of the Duschinsky parameters

Eq. (22) expresses the possibly different equilibrium positions in the electronic ground and excited states, as well as the different relative orientations of the vibrational eigenmodes. For a N -atom system, and denoting by $\mathbf{x} = (x_1, \dots, x_{3N})$ the set of $3N$ molecular mass-scaled rectilinear coordinates, the electronic ground state potential energy surface is expanded around its equilibrium position \mathbf{x}_g as

$$V_g(\mathbf{x}) \approx \frac{1}{2} (\mathbf{x}^T - \mathbf{x}_g^T) \mathbf{V}_g (\mathbf{x} - \mathbf{x}_g), \quad (\text{B1})$$

where \mathbf{V}_g is the force constant matrix. We further denote by \mathbf{K}_g the $3N \times n$ matrix composed of the $n = 3N - 6$ vibrational eigenstates of \mathbf{V}_g , and write the ground state vibrational normal modes as

$$\mathbf{x} = \mathbf{x}_g + \mathbf{K}_g \mathbf{q}_g. \quad (\text{B2})$$

A similar harmonic expansion can be performed in the electronic excited state,

$$V_e(\mathbf{x}) \approx \frac{1}{2} (\mathbf{x}^T - \mathbf{x}_e^T) \mathbf{V}_e (\mathbf{x} - \mathbf{x}_e) + \hbar\omega_{eg}, \quad (\text{B3})$$

where the equilibrium coordinates \mathbf{x}_e are expressed in the Eckart frame with respect to the electronic ground state equilibrium geometry \mathbf{x}_g . Similarly as with the electronic ground state, the $3N \times n$ matrix \mathbf{K}_e is introduced, combining the n vibrational eigenstates of \mathbf{V}_e , allowing the electronic excited state vibrational normal modes to be defined as

$$\mathbf{x} = \mathbf{x}_e + \mathbf{K}_e \mathbf{q}_e. \quad (\text{B4})$$

The Duschinsky relation connecting \mathbf{q}_g and \mathbf{q}_e to each other is then given by

$$\mathbf{q}_e = \mathbf{K}_e^T \mathbf{K}_g \mathbf{q}_g + \mathbf{K}_e^T (\mathbf{x}_g - \mathbf{x}_e), \quad (\text{B5})$$

from which the expression for the Duschinsky rotation matrix \mathbf{S} and the displacement vector \mathbf{K} can be readily obtained as

$$\mathbf{S} = \mathbf{K}_e^T \mathbf{K}_g, \quad (\text{B6})$$

and

$$\mathbf{K} = \mathbf{K}_e^T (\mathbf{x}_g - \mathbf{x}_e), \quad (\text{B7})$$

respectively.

Appendix C: Validity of the harmonic and HT approximations

The model for RF relaxation relies on the potential energy and transition dipole moment surfaces being correctly described by harmonic and linear expressions, respectively. Here we examine the quality of these approximations on selected electronic states of the three PAH cations. Starting from the D_1 electronic excited state minimum geometry, a deformation was applied by following a specific eigenvector $q_{e,k}$ associated with mode k . Because the extent of molecular deformation depends on the amount of energy injected in the molecule, a maximum deformation amplitude $q_{e,k}^{\max}$ was imposed as $2\sqrt{\langle q_{e,k}^2 \rangle}$, where the canonical average $\langle \cdot \rangle$ is taken at a physically relevant temperature T . In the harmonic approximation, this average depends on the mode frequency $\omega_{e,k}$ through

$$\langle q_{e,k}^2 \rangle = \frac{\hbar}{2\omega_{e,k}} \coth\left(\frac{\hbar\omega_{e,k}}{2k_B T}\right). \quad (\text{C1})$$

Fig. 10 shows the variations of the electronic excited state energy (relative to the minimum) and the transition dipole moment between the electronic ground and excited states, as a function of the normal mode coordinates $q_{e,k}$ and for selected modes of the three PAH cations, notably the modes

having the highest contribution to the HT oscillator strength, as well as the lowest-frequency A_u vibrational modes. In each graph, the values obtained from the TD-DFT calculations are compared with the predictions of the harmonic (energy) or linear (transition dipole moment) approximations for the corresponding quantities. For the transition dipole moment, which is a vectorial quantity, only the component that acquires a nonvanishing value after applying the deformation was considered. This component depends on the cation itself and on the symmetry of the normal mode.

In the case of Np^+ , and except for the softest A_u mode $q_{e,1}$, the agreement between the direct calculation and the model system is very good, with almost indistinguishable differences. In the specific case of $q_{e,1}$ for Np^+ , and for large deformation amplitudes, the D_0 and D_1 electronic states cross each other. As a result, for large deformations $|q_{e,1}| \gtrsim 150$ a.u. the electronic ground state becomes the state with symmetry $^2\text{B}_{3u}$, while the electronic excited state switches to $^2\text{A}_u$ symmetry. This crossing at the origin of a conical intersection between the D_1 and D_0 states in Np^+ has been discussed earlier.^{48,61} Alongside the other conical intersections between the various electronic states of Np^+ and other PAHs, these features justify our statistical model in the microcanonical ensemble, energy redistribution between all electronic states occurring on fast time scales. In the case of An^+ and Py^+ , a similarly good agreement is found between the harmonic model and the TD-DFT calculations, with the exception of the lowest-frequency A_u vibrational modes. In these cases, and while no crossing occurs between electronic states, very large intramode anharmonicities are found. Note that, as shown in Fig. 5, all these low-frequency A_u vibrational modes contribute only slightly to the overall HT oscillator strength.

ACKNOWLEDGMENTS

Financial support by the ANR "INTERSTELLAR" under Grant No. ANR-23-CE30-0023 is acknowledged. The authors would like to acknowledge M. H. Stockett, H. Zettergren and J. N. Bull for useful discussions. This work was performed using computational resources from the "Mésocentre" computing center of Université Paris-Saclay, CentraleSupélec and École Normale Supérieure Paris-Saclay supported by CNRS and Région Île-de-France (<https://mesocentre.universite-paris-saclay.fr/>).

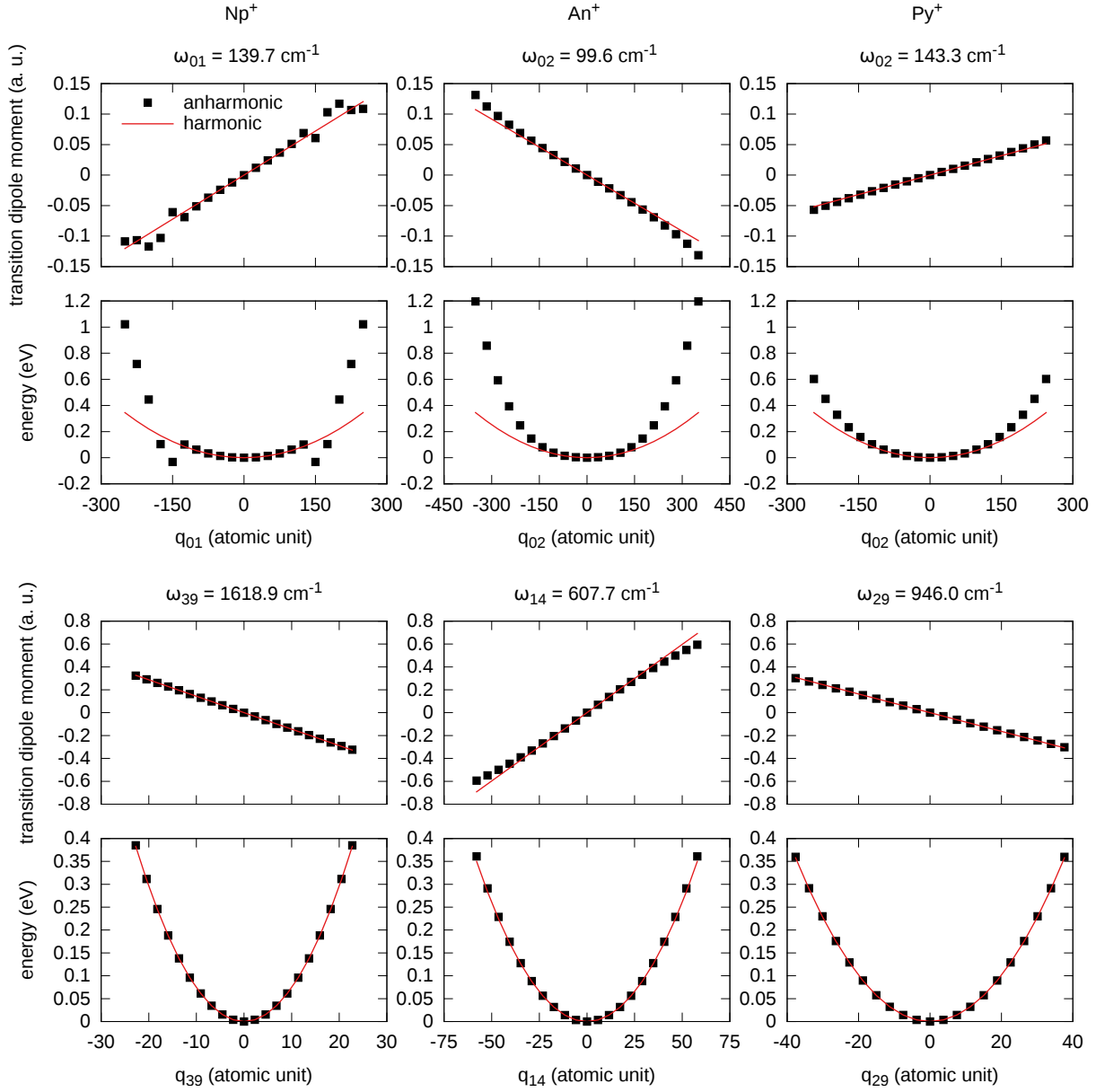


FIG. 10. Comparison between TD-DFT calculations and the harmonic approximation for the energy of the D_1 electronic state and the linear approximation for the transition dipole moment along various normal mode coordinates of the naphthalene (left panels), anthracene (middle panels), and pyrene (right panels) cations.

AUTHOR DECLARATION SECTION

Conflict of Interest Statement

The authors have no conflicts to disclose.

Author Contributions

Damien Borja: Conceptualization (equal); Formal Analysis (lead); Investigation (equal); Methodology (equal); Software (equal); Visualization (lead); Writing – Original Draft Preparation (equal); Writing – Review & Editing (equal) **Florent Calvo:** Conceptualization (equal); Methodology (supporting); Writing – Review & Editing (equal) **Pascal Parneix:** Conceptualization (equal); Funding Acquisition (equal); Methodology (supporting); Writing – Review & Editing (equal) **Cyril Falvo:** Conceptualization (equal); Funding Acquisition (equal); Investigation (equal); Methodology (equal); Software (equal); Supervision (lead); Writing – Original Draft Preparation (equal); Writing – Review & Editing (equal)

DATA AVAILABILITY

The data that support the findings of this study are available from the corresponding author upon reasonable request.

REFERENCES

- ¹A. Léger and J. L. Puget, “Identification of the ‘unidentified’ IR emission features of interstellar dust?” *Astron. Astrophys.* **137**, L5–L8 (1984).
- ²L. J. Allamandola, A. G. G. M. Tielens, and J. R. Barker, “Polycyclic aromatic hydrocarbons and the unidentified infrared emission bands - auto exhaust along the Milky Way,” *Astrophys. J.* **290**, L25–L28 (1985).
- ³B. A. McGuire, R. A. Loomis, A. M. Burkhardt, K. L. K. Lee, C. N. Shingledecker, S. B. Charnley, I. R. Cooke, M. A. Cordiner, E. Herbst, S. Kalenskii, M. A. Siebert, E. R. Willis, C. Xue, A. J. Remijan, and M. C. McCarthy, “Detection of two interstellar polycyclic aromatic hydrocarbons via spectral matched filtering,” *Science* **371**, 1265–1269 (2021).

⁴H. W. Jochims, H. Baumgärtel, and S. Leach, “Structure-dependent photostability of polycyclic aromatic hydrocarbon cations: Laboratory studies and astrophysical implications,” *Astrophys. J.* **512**, 500 (1999).

⁵A. Léger, P. Boissel, and L. d’Hendecourt, “Predicted fluorescence mechanism in highly isolated molecules: The Poincaré fluorescence,” *Phys. Rev. Lett.* **60**, 921–924 (1988).

⁶K. Sellgren, M. W. Werner, and H. L. Dinerstein, “Extended near-infrared emission from visual reflection nebulae.” *Astrophys. J.* **271**, L13–L17 (1983).

⁷Z. Karny, A. Gupta, R. N. Zare, S. T. Lin, J. Nieman, and A. M. Ronn, “Collisionless infrared multiphoton production of electronically excited parent molecules,” *Chem. Phys.* **37**, 15–20 (1979).

⁸O. Lacinbala, F. Calvo, E. Dartois, C. Falvo, P. Parneix, A. Simon, and T. Pino, “A plausible molecular mechanism to explain near-infrared continuum emission: Recurrent fluorescence,” *Astron. Astrophys.* **671**, A89 (2023).

⁹P. Boissel, P. de Parseval, P. Marty, and G. Lefevre, “Fragmentation of isolated ions by multiple photon absorption: A quantitative study,” *J. Chem. Phys.* **106**, 4973–4984 (1997).

¹⁰M. Saito, H. Kubota, K. Yamasa, K. Suzuki, T. Majima, and H. Tsuchida, “Direct measurement of recurrent fluorescence emission from naphthalene ions,” *Phys. Rev. A* **102**, 012820 (2020).

¹¹J. Kusuda, R. Fukuzaki, T. Majima, H. Tsuchida, and M. Saito, “Detection of recurrent fluorescence from anthracene using an electrostatic ion beam trap,” *Nucl. Instrum. Methods Phys. Res. B: Beam Interact. Mater. At.* **553**, 165387 (2024).

¹²S. Martin, J. Bernard, R. Brédy, B. Concina, C. Joblin, M. Ji, C. Ortega, and L. Chen, “Fast radiative cooling of anthracene observed in a compact electrostatic storage ring,” *Phys. Rev. Lett.* **110**, 063003 (2013).

¹³S. Martin, M. Ji, J. Bernard, R. Brédy, B. Concina, A. R. Allouche, C. Joblin, C. Ortega, G. Montagne, A. Cassimi, Y. Ngono-Ravache, and L. Chen, “Fast radiative cooling of anthracene: Dependence on internal energy,” *Phys. Rev. A* **92**, 053425 (2015).

¹⁴S. Martin, J. Matsumoto, N. Kono, M. C. Ji, R. Brédy, J. Bernard, A. Cassimi, and L. Chen, “Fluorescence decay of naphthalene studied in an electrostatic storage ring, the mini-ring,” *Nucl. Instrum. Methods Phys. Res. B: Beam Interact. Mater. At.* **408**, 209–212 (2017).

¹⁵J. Bernard, L. Chen, R. Brédy, M. Ji, C. Ortéga, J. Matsumoto, and S. Martin, “Cooling of PAH cations studied with an electrostatic storage ring,” *Nucl. Instrum. Methods Phys. Res. B: Beam Interact. Mater. At.* **408**, 21–26 (2017).

¹⁶J. Bernard, M. Ji, S. Indrajith, M. H. Stockett, J. E. Navarro Navarrete, N. Kono, H. Cederquist, S. Martin, H. T. Schmidt, and H. Zettergren, “Efficient radiative cooling of tetracene cations $C_{18}H_{12}^+$: absolute recurrent fluorescence rates as a function of internal energy,” *Phys. Chem. Chem. Phys.* **25**, 10726–10740 (2023).

¹⁷J. W. L. Lee, M. H. Stockett, E. K. Ashworth, J. E. Navarro Navarrete, E. Gougoula, D. Garg, M. Ji, B. Zhu, S. Indrajith, H. Zettergren, H. T. Schmidt, and J. N. Bull, “Cooling dynamics of energized naphthalene and azulene radical cations,” *J. Chem. Phys.* **158**, 174305 (2023).

¹⁸M. H. Stockett, J. N. Bull, H. Cederquist, S. Indrajith, M. Ji, J. Navarro Navarrete, H. T. Schmidt, H. Zettergren, and B. Zhu, “Efficient stabilization of cyanonaphthalene by fast radiative cooling and implications for the resilience of small PAHs in interstellar clouds,” *Nature Commun.* **14**, 395 (2023).

¹⁹J. N. Bull, A. Subramani, C. Liu, S. J. P. Marlton, E. K. Ashworth, H. Cederquist, H. Zettergren, and M. H. Stockett, “Radiative stabilization of the indenyl cation: Recurrent fluorescence in a closed-shell polycyclic aromatic hydrocarbon,” *Phys. Rev. Lett.* **134**, 228002 (2025).

²⁰B. West, C. Joblin, V. Blanchet, A. Bodi, B. Sztáray, and P. M. Mayer, “On the dissociation of the naphthalene radical cation: New iPEPICO and tandem mass spectrometry results,” *J. Phys. Chem. A* **116**, 10999–11007 (2012).

²¹B. West, F. Useli-Bacchitta, H. Sabbah, V. Blanchet, A. Bodi, P. M. Mayer, and C. Joblin, “Photodissociation of pyrene cations: Structure and energetics from $C_{16}H_{10}^+$ to C_{14}^+ and almost everything in between,” *J. Phys. Chem. A* **118**, 7824–7831 (2014).

²²B. West, S. Rodriguez Castillo, A. Sit, S. Mohamad, B. Lowe, C. Joblin, A. Bodi, and P. M. Mayer, “Unimolecular reaction energies for polycyclic aromatic hydrocarbon ions,” *Phys. Chem. Chem. Phys.* **20**, 7195–7205 (2018).

²³A. Nitzan and J. Jortner, “Inverse electronic relaxation,” *Chem. Phys. Lett.* **60**, 1–4 (1978).

²⁴A. Nitzan and J. Jortner, “Theory of inverse electronic relaxation,” *J. Chem. Phys.* **71**, 3524–3532 (1979).

²⁵V. Chandrasekaran, B. Kafle, A. Prabhakaran, O. Heber, M. Rappaport, H. Rubinstein, D. Schwalm, Y. Toker, and D. Zajfman, “Determination of absolute recurrent fluorescence rate coefficients for C_6^- ,” *J. Phys. Chem. Lett.* **5**, 4078–4082 (2014).

²⁶O. Lacinbala, F. Calvo, C. Dubosq, C. Falvo, P. Parneix, M. Rapacioli, A. Simon, and T. Pino, “Radiative relaxation in isolated large carbon clusters: Vibrational emission versus recurrent fluorescence,” *J. Chem. Phys.* **156**, 144305 (2022).

²⁷H. B. Pedersen and L. H. Andersen, “Spectroscopy and recurrent fluorescence from cryogenically cooled C₄⁻,” Phys. Rev. A **112**, 022820 (2025).

²⁸O. Lacinbala, F. Calvo, C. Falvo, P. Parneix, M. Rapacioli, A. Simon, and T. Pino, “Emission spectra of fullerenes: Computational evidence for blackbody-like radiation due to structural diversity and electronic similarity,” Phys. Rev. A **107**, 062808 (2023).

²⁹G. Herzberg, *Molecular Spectra and Molecular Structure*, Vol. III. Electronic Spectra and Electronic Structure of Polyatomic Molecules (D. Van Nostrand Company, Inc., 1966).

³⁰S. Kundu, P. P. Roy, G. R. Fleming, and N. Makri, “Franck-Condon and Herzberg-Teller signatures in molecular absorption and emission spectra,” J. Phys. Chem. B **126**, 2899–2911 (2022).

³¹J. Weber and G. Hohlneicher, “Franck-Condon factors for polyatomic molecules,” Mol. Phys. **101**, 2125–2144 (2003).

³²J. Huh and R. Berger, “Coherent state-based generating function approach for Franck-Condon transitions and beyond,” J. Phys. Conf. Ser. **380**, 012019 (2012).

³³Y. J. Yan and S. Mukamel, “Eigenstate-free, Green function, calculation of molecular absorption and fluorescence line shapes,” J. Chem. Phys. **85**, 5908–5923 (1986).

³⁴R. Ianconescu and E. Pollak, “Photoinduced cooling of polyatomic molecules in an electronically excited state in the presence of Dushinskii rotations,” J. Phys. Chem. A **108**, 7778–7784 (2004).

³⁵A. Baiardi, J. Bloino, and V. Barone, “General time dependent approach to vibronic spectroscopy including Franck-Condon, Herzberg-Teller, and Duschinsky effects,” J. Chem. Theory Comput. **9**, 4097–4115 (2013).

³⁶S. Hirata, M. Head-Gordon, J. Szccepanski, and M. Vala, “Time-dependent density functional study of the electronic excited states of polycyclic aromatic hydrocarbon radical ions,” J. Phys. Chem. A **107**, 4940–4951 (2003).

³⁷A. Subramani, J. N. Bull, H. Cederquist, P. Martini, H. T. Schmidt, H. Zettergren, and M. H. Stockett, “Recurrent fluorescence of polycyclic aromatic hydrocarbon isomers: A comparative study,” ACS Earth Space Chem. **in press** (2025), 10.1021/acsearthspacechem.5c00283.

³⁸J. Zinn-Justin, *Path Integrals in Quantum Mechanics* (Oxford University Press, Oxford, 2005).

³⁹J. Szccepanski, M. Vala, D. Talbi, O. Parisel, and Y. Ellinger, “Electronic and vibrational spectra of matrix isolated anthracene radical cations: Experimental and theoretical aspects,” J. Chem. Phys. **98**, 4494–4511 (1993).

⁴⁰M. Vala, J. Szczepanski, F. Pauzat, O. Parisel, D. Talbi, and Y. Ellinger, “Electronic and vibrational spectra of matrix-isolated pyrene radical cations: Theoretical and experimental aspects,” *J. Phys. Chem.* **98**, 9187–9196 (1994).

⁴¹T. Bally, C. Carra, M. P. Fülscher, and Z. Zhu, “Electronic structure of the naphthalene radical cation and some simple alkylated derivatives,” *J. Chem. Soc. Perkin Trans. 2*, 1759–1766 (1998).

⁴²F. Negri and M. Z. Zgierski, “On the vibronic structure of the absorption spectra of radical cations of some polycyclic aromatic hydrocarbons,” *J. Chem. Phys.* **100**, 1387–1399 (1994).

⁴³F. Negri and M. Z. Zgierski, “Theoretical analysis of the vibronic structure of the zero-kinetic-energy photoelectron spectra from single vibronic levels of the S₁-state manifold of naphthalene,” *J. Chem. Phys.* **107**, 4827–4843 (1997).

⁴⁴S. Hirata, T. J. Lee, and M. Head-Gordon, “Time-dependent density functional study on the electronic excitation energies of polycyclic aromatic hydrocarbon radical cations of naphthalene, anthracene, pyrene, and perylene,” *J. Chem. Phys.* **111**, 8904–8912 (1999).

⁴⁵G. Mallocci, G. Mulas, and C. Joblin, “Electronic absorption spectra of PAHs up to vacuum UV - towards a detailed model of interstellar PAH photophysics,” *Astron. Astrophys.* **426**, 105–117 (2004).

⁴⁶G. Mallocci, G. Mulas, G. Cappellini, and C. Joblin, “Time-dependent density functional study of the electronic spectra of oligoacenes in the charge states -1, 0, +1, and +2,” *Chem. Phys.* **340**, 43–58 (2007).

⁴⁷G. Mallocci, G. Cappellini, G. Mulas, and A. Mattoni, “Electronic and optical properties of families of polycyclic aromatic hydrocarbons: A systematic (time-dependent) density functional theory study,” *Chem. Phys.* **384**, 19–27 (2011).

⁴⁸M. Boggio-Pasqua and M. J. Bearpark, “Using density functional theory based methods to investigate the photophysics of polycyclic aromatic hydrocarbon radical cations: A benchmark study on naphthalene, pyrene and perylene cations,” *ChemPhotoChem* **3**, 763–769 (2019).

⁴⁹I. Knysh, F. Lipparini, A. Blondel, I. Duchemin, X. Blase, P.-F. Loos, and D. Jacquemin, “Reference CC3 excitation energies for organic chromophores: Benchmarking TD-DFT, BSE/GW, and wave function methods,” *J. Chem. Theory Comput.* **20**, 8152–8174 (2024).

⁵⁰M. E. Casida, C. Jamorski, K. C. Casida, and D. R. Salahub, “Molecular excitation energies to high-lying bound states from time-dependent density-functional response theory: Characterization and correction of the time-dependent local density approximation ionization threshold,” *J. Chem. Phys.* **108**, 4439–4449 (1998).

⁵¹M. Casida and M. Huix-Rotllant, “Progress in time-dependent density-functional theory,” *Annu. Rev. Phys. Chem.* **63**, 287–323 (2012).

⁵²J.-D. Chai and M. Head-Gordon, “Long-range corrected hybrid density functionals with damped atom-atom dispersion corrections,” *Phys. Chem. Chem. Phys.* **10**, 6615–6620 (2008).

⁵³T. H. Dunning, Jr., “Gaussian basis sets for use in correlated molecular calculations. I. the atoms boron through neon and hydrogen,” *J. Chem. Phys.* **90**, 1007–1023 (1989).

⁵⁴R. A. Kendall, T. H. Dunning, and R. J. Harrison, “Electron affinities of the first-row atoms revisited. Systematic basis sets and wave functions,” *J. Chem. Phys.* **96**, 6796–6806 (1992).

⁵⁵M. J. Frisch, G. W. Trucks, H. B. Schlegel, G. E. Scuseria, M. A. Robb, J. R. Cheeseman, G. Scalmani, V. Barone, G. A. Petersson, H. Nakatsuji, X. Li, M. Caricato, A. V. Marenich, J. Bloino, B. G. Janesko, R. Gomperts, B. Mennucci, H. P. Hratchian, J. V. Ortiz, A. F. Izmaylov, J. L. Sonnenberg, D. Williams-Young, F. Ding, F. Lipparini, F. Egidi, J. Goings, B. Peng, A. Petrone, T. Henderson, D. Ranasinghe, V. G. Zakrzewski, J. Gao, N. Rega, G. Zheng, W. Liang, M. Hada, M. Ehara, K. Toyota, R. Fukuda, J. Hasegawa, M. Ishida, T. Nakajima, Y. Honda, O. Kitao, H. Nakai, T. Vreven, K. Throssell, J. A. Montgomery, Jr., J. E. Peralta, F. Ogliaro, M. J. Bearpark, J. J. Heyd, E. N. Brothers, K. N. Kudin, V. N. Staroverov, T. A. Keith, R. Kobayashi, J. Normand, K. Raghavachari, A. P. Rendell, J. C. Burant, S. S. Iyengar, J. Tomasi, M. Cossi, J. M. Millam, M. Klene, C. Adamo, R. Cammi, J. W. Ochterski, R. L. Martin, K. Morokuma, O. Farkas, J. B. Foresman, and D. J. Fox, “Gaussian 16 Revision B.01,” (2016), Gaussian Inc. Wallingford CT.

⁵⁶S. E. Stein and B. S. Rabinovitch, “Accurate evaluation of internal energy level sums and densities including anharmonic oscillators and hindered rotors,” *J. Chem. Phys.* **58**, 2438–2445 (1973).

⁵⁷T. Beyer and D. F. Swinehart, “Algorithm 448: number of multiply-restricted partitions,” *Commun. ACM* **16**, 379 (1973).

⁵⁸R. Boschi, J. N. Murrell, and W. Schmidt, “Photoelectron spectra of polycyclic aromatic hydrocarbons,” *Faraday Discuss. Chem. Soc.* **54**, 116–126 (1972).

⁵⁹R. Boschi and W. Schmidt, “Photoelectron spectra of polycyclic aromatic hydrocarbons. pyrene and coronene,” *Tetrahedron Lett.* **13**, 2577–2580 (1972).

⁶⁰P. M. Mayer, V. Blanchet, and C. Joblin, “Threshold photoelectron study of naphthalene, anthracene, pyrene, 1,2-dihydronaphthalene, and 9,10-dihydroanthracene,” *J. Chem. Phys.* **134**, 244312 (2011).

⁶¹A. M. Tokmachev, M. Boggio-Pasqua, M. J. Bearpark, and M. A. Robb, “Photostability via sloped conical intersections: A computational study of the pyrene radical cation,” *J. Phys. Chem. A* **112**, 10881–10886 (2008).